Radiative Capture of Tensor and Vector Polarized Deuterons by Tritium at 8.6 MeV and 400 keV

by

John Charles Riley

Department of Physics
Duke University

Date: September 18, 1989

Approved:

_____

Henry R. Weller, Supervisor

_____

_____

_____

_____

Dissertation submitted in partial fulfillment of the requirements for the degree of Doctor of Philosophy in the Department of Physics in the Graduate School of Duke University

1989

ABSTRACT

(Physics-Nuclear)

Radiative Capture of Tensor and Vector Polarized Deuterons by Tritium at 8.6 MeV and 400 keV

by

John Charles Riley

Department of Physics
Duke University

Date: September 18, 1989

Approved:

_____

Henry R. Weller, Supervisor

_____

_____

_____

_____

An abstract of a dissertation submitted in partial fulfillment of the requirements for the degree of Doctor of Philosophy in the Department of Physics in the Graduate School of Duke University

1989

Abstract

The $^{3}H(d,\gamma)^{5}He$ reaction was studied at 8.6 MeV and 400 keV using polarized and unpolarized beams to deduce the relative strengths of the S =3/2 and S =1/2 channels. The absolute differential cross section $\sigma(\theta)$, $A_y(\theta)$, and $T_{20}(\theta)$ were measured at E_d=8.6 MeV and the differential cross section $\sigma(\theta)$, $A_y(\theta)$, and $A_{yy}(\theta)$ were measured at 400 keV.

The a_k, b_k, and c_k coefficients of Legendre polynomial expansions of the observables were extracted at both energies. A T-matrix analysis of the E_d= 400keV data indicates 95% S = 3/2 (E1) strength, with 2.5% S =1/2 (E1) and 2.5% M1 strength present.

A direct capture E1 calculation was performed at 8.6 MeV and was in good agreement with the experimentally determined coefficients when a spin-orbit interaction was included. The results of this comparison indicated that the ground state of ^{5}He consisted of 88-100% S =3/2 strength. This result was also consistent with the 95% S =3/2 (E1) strength found by the T-matrix analysis of the low energy data.

This dissertation is dedicated to
my family,
who alway believed in me and encouraged me
in all my endeavors for these many years.

Thanks most of all to Dr. Grace Mendez, my wife, for all of the love and support she has given me over the last three years. Without her this dissertation could never have come to fruition.

I also thank my advisor, Dr. Henry R. Weller, for giving me a chance when others would not and standing by me in times of need. His support and contributions to my education have been tremendous and much appreciated.

Many thanks go to the other members of the capture group, past and present, who have contributed towards this work: Dr. Ron Tilley, Dr. Gerald Feldman, Dr. Paul Colby, Dr. V. Wijekumar, Dr. Z.D. Huang, Dr. Michael Wright, Dr. Steven King, Dr. Bob August, Dr. George Mitev, Dr. Doug Wagenaar, James Langenbrunner, Zandy Williams, and Mark Balbes. Special thanks to Laird Kramer who helped me a great deal with some difficult calculations and to Dr. Mark Whitton who has been a good friend, colleague and classmate for these last seven years.

Last of all, I would like to thank the U.S. Department of Energy for their continued support of non-defense related research that has made my education financially possible.

Table of Contents

List of Figures

List of Tables

Chapter 1

Introduction

The capture reaction $^{3}H(d,\gamma)^{5}He$ has been a largely unexamined reaction despite the relative simplicity of the A=5 system. Previous work on the reaction was performed with unpolarized beams measuring cross sections and $\sigma(d,\gamma)/\sigma(d,n)$ branching ratios below E_d = 1 MeV [Buss, 1963; Kosiara, 1970; Bezotsnyi, 1975; Cecil, 1985; Morgan, 1986] and cross section measurements for E_d = 2-12 MeV [Batay-Csorba, 1975]. Angular distributions have not been measured before. There have also been no previous studies of this reaction using polarized beams, a need which the present work attempts to fill.

$^{3}H(d,\gamma)^{5}He$ is a difficult reaction technically to make measurements on because of several factors. First, tritium is a highly radioactive gas that is difficult to make into a suitable target that can be safely handled and stored. The targets used in these experiments were tritiated titanium foils for ease of handling and to minimize safety concerns, although at the expense of having the spectra contaminated by background resulting from the titanium. Another difficulty in this experiment is the tremendous neutron flux produced in the $^{3}H(d,n)^{4}He$ reaction, especially at the lower energy measured here and at forward angles at 8.6 MeV. The techniques of handling this problem are addressed in Chapter 2.

Both polarized and unpolarized beams were used at 8.6 MeV and 400 keV to measure tensor and vector analyzing powers of the reaction, an absolute differential cross section at 8.6 MeV and a differential cross section at 400 keV. The objectives were to deduce how much strength was carried by each of the channels of the reaction and to gain

insight into the spin structure of the ground state of ^{5}He. Polarized beams have proven themselves to be very powerful tools in investigating light nuclei, and made it possible to understand much about the ^{3}H(d,γ)^{5}He reaction.

This dissertation will describe the methods used to investigate the ^{3}H(d,γ)^{5}He reaction, present the results of this investigation, interpret those results, and draw conclusions from them.

Chapter 2

Experimental Techniques and Equipment

2.1 Introduction

The data in this thesis were taken at TUNL; a schematic diagram showing the layout of the laboratory is shown in Figure 2-1. Polarized and unpolarized deuterons incident on a tritiated Titanium foil were used to study the $^{3}H(d,\gamma)^{5}He$ reaction at E_d= 8.6 MeV and 400 keV. The absolute differential cross section, $T_{20}(\theta)$ and $A_y(\theta)$ were measured at seven angles in the experiment at 8.6 MeV. In the experiments at 400 keV, the differential cross section was measured at nine angles, and $A_{yy}(\theta)$ and $A_y(\theta)$ were measured at seven angles. Polarized deuterons were supplied by the TUNL Polarized Ion Source (PIS) and the unpolarized deuterons were supplied by the TUNL Direct Extraction Negative Ion Source (DENIS). The deuterons were accelerated by a Type FN Tandem Van de Graaff accelerator. The operation and characteristics of the ion sources and accelerators have been described in publications [Newson, 1974; Clegg, 1974]. The resulting γ-rays were detected by two 25.4 cm x 25.4 cm cylindrical NaI detectors. The following sections of this chapter deal with the beam transportation, detectors involved, targets used, and electronic and software sorting techniques used to obtain the desired γ-ray spectra.

2.2) Beam

Both the unpolarized and polarized beams were pulsed prior to injection into the Tandem Van de Graaff. The unpolarized deuterons were passed through a radio frequency

Figure 2-1: Triangle Universities Nuclear Laboratory

Triangle Universities Nuclear Laboratory (TUNL)

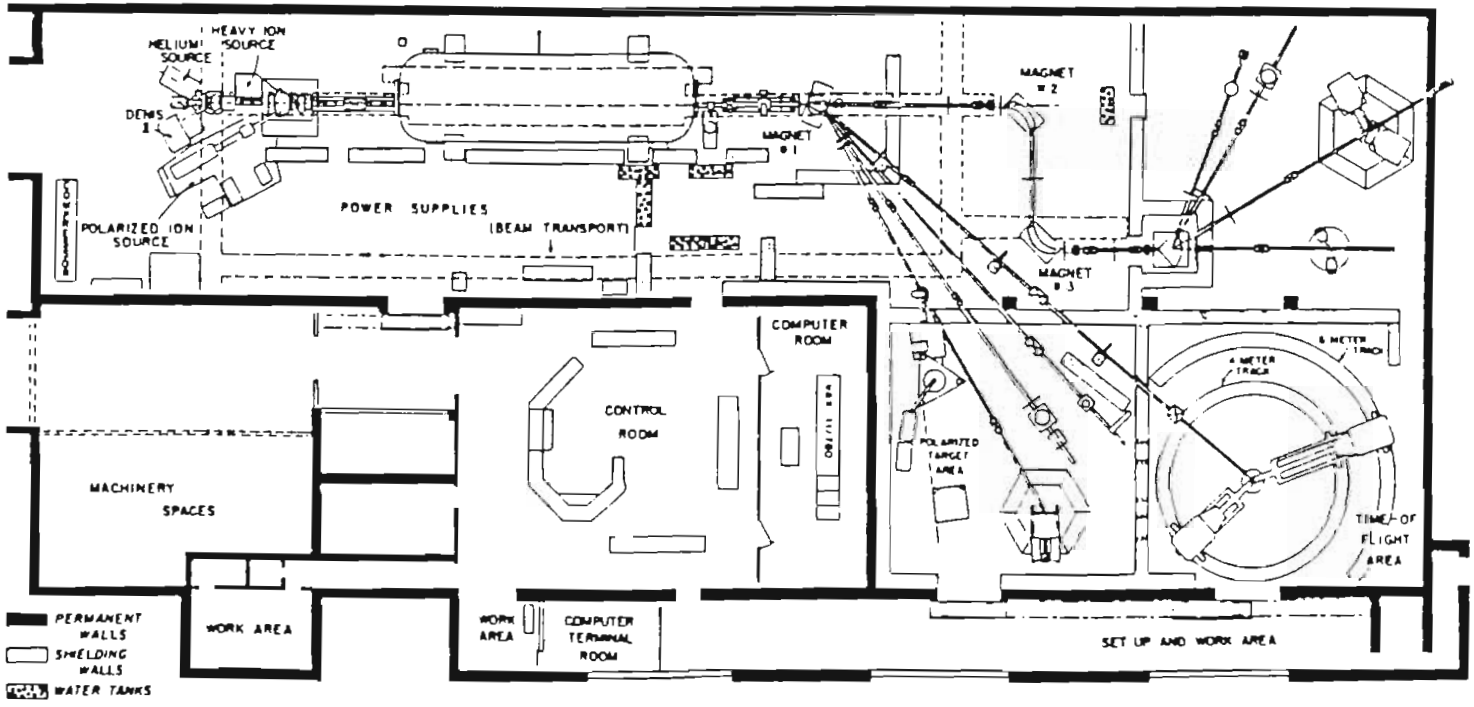

chopper and a double drift buncher, producing a 2 ns beam burst with a repetition rate of 2 MHz. The polarized deuterons were ramped in the duoplasmatron of the source, then sent through a double drift buncher and a chopper [Wender, 1980], producing a beam burst of 2-3 ns at a repetition rate of 4 MHz. The beams were then accelerated through a model FN tandem Van de Graaff. After acceleration, the beam passed through a pair of 90 degree magnets used for energy analysis and a 30 degree switching magnet to get to target room 4 (Figure 2-1), where the experimental area was located. At a point just before the target chamber, the beam passed through a 7.6 cm long x 1.0 cm diameter copper tube serving as a capacitive pickup, providing a stop signal for a time-to-amplitude converter used for time-of-flight measurements. In the experiments done at 8.6 MeV, the beam then passed through a 0.25 cm diameter hole in a tantalum disk for collimation, passed through the target foil and into the tantalum Faraday cup, which was located 2 m behind the laboratory wall. The collimator current was minimized and usually kept in the 1 to 2 nA range. Beam currents on target ranged from 60 to 100 nA in the case of polarized beam, with a typical polarization of 60 %, measured by the quench-ratio method before the first 90 degree magnet. Beam current was limited to 140 nA in the case of unpolarized beam because of count rate limitations in the NaI spectrometers. The integrated beam currents were used for cross section determination and relative normalization.

In the low energy experiments, a 3.375 MeV beam was passed through the same system as in the 8.6 MeV experiment until after the capacitive pickup. The beam then passed through a 0.4 cm diameter hole in a tantalum collimator, an electron suppression ring, a 1 mil Havar energy degrading foil, and was finally stopped in the target foil. The beam

energy after the degrading foil was approximately 400 keV with an energy spread of 200 keV FWHM (Figure 2-2). The procedure for degrading the beam and determining its energy and energy spread is described in section 2.7). The collimator current was usually held to less than 1 nA. The electron suppression ring and a small 2" diameter chamber (Figure 2-3) allowed us to integrate the beam on target for the purpose of relative normalization. Typical beam currents were similar to that above for unpolarized beam, but only 60 nA for the polarized beam because of the lower transmission through the accelerator at lower terminal voltages.

2.3) Detectors

Two 25.4 cm x 25.4 cm cylindrical NaI scintillators surrounded by NE 110 plastic [Suffert, 1968] anti-coincidence shields were used to detect the γ-rays in this experiment. These detectors were surrounded by 20 cm of lithium carbonate doped paraffin (50 % by weight) and 10 cm of lead. The paraffin moderates the neutron flux which is then attenuated by the high cross section for the $^{6}Li(n,\alpha)$ reaction at thermal neutron energies. Both detectors also had a 0.6 cm thick sheet of boron carbide doped plastic (50 % by weight) between the paraffin and lead and the right detector had a 0.15 cm sheet of cadmium in front of the boron doped plastic. Both boron and cadmium have high cross sections for thermal neutron absorption and were used for thermal neutron attenuation, having an attenuation factor of 10^{11}. Each detector had a tapered lead collimator that illuminated the rear face of the NaI crystal which was positioned at a distance of 108 cm from the center of the target chamber. The

Figure 2-2:Solid state detector spectrum of elastically scattered deuterons after passing through the degrading foil.

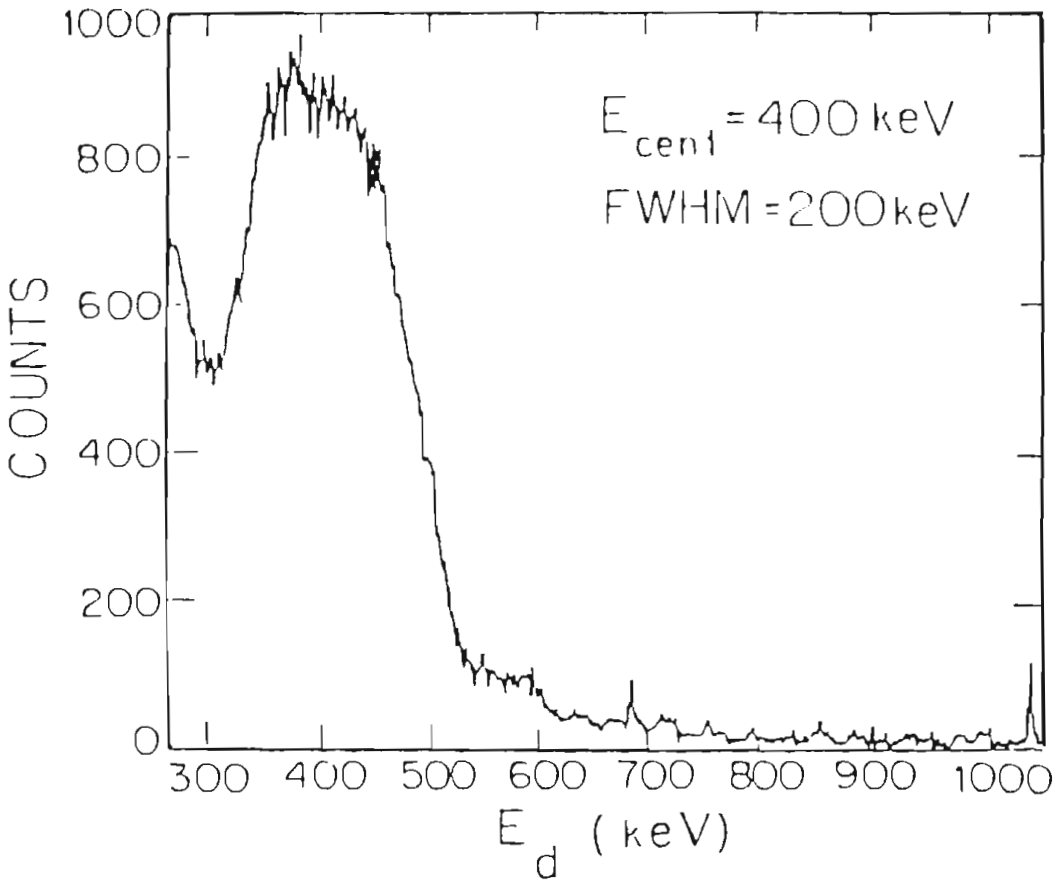
1000
800
600
400
200
0
COUNTS
E_{cent} = 400 keV
FWHM = 200 keV
300 400 500 600 700 800 900 1000
E_d (keV)

Figure 2-3:Chamber used in experiments at 400 keV. The diameter of the chamber is two inches.

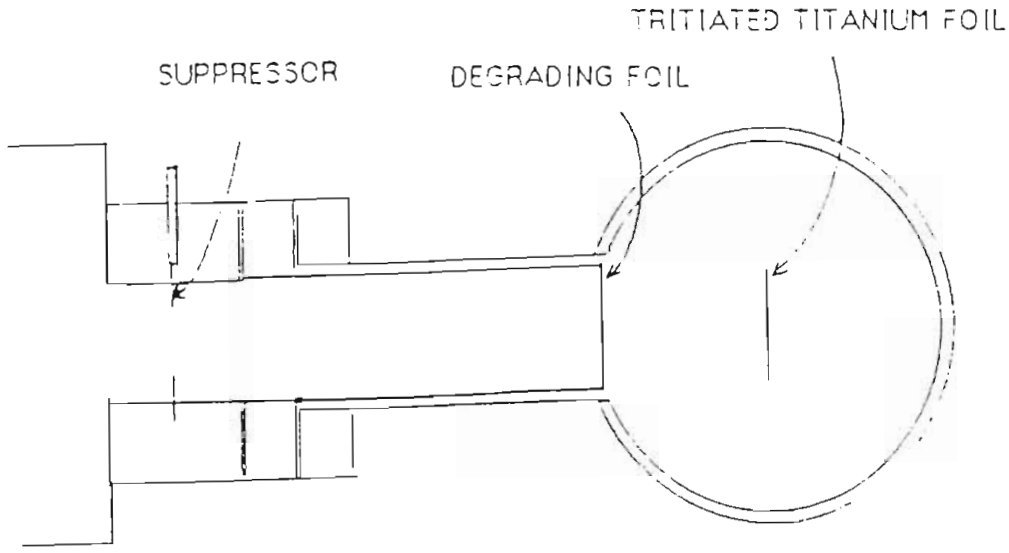
TRITIATED TITANIUM FOIL
SUPPRESSOR
DEGRADING FOIL

resolution of each of these systems was about 3 % for the 16.8 to 22.4 MeV γ-rays in these experiments [Weller, 1980]. The detection system for the experiment at E_d=8.6 MeV is shown in Figure 2-4. In the experiment at E_d=400 keV, tungsten shadow bars were used to shield the detectors from the energy degrading foil.

2.4) Monitor detectors

A silicon surface barrier detector was used as a monitor in the E_d=8.6 MeV experiments. It was placed at forward angles from 50 to 70 degrees from the beam direction. The detector thicknesses used varied from 500 to 1500 microns, depending on the beam energy. Elastically scattered deuterons from tritium and titanium as well as recoil tritons were observed. Tantalum collimators with small holes in them were placed 2.5 cm from and directly in front of the detector. In the low energy experiments, a NE213 scintillator with tapered copper collimators was placed 260 cm from the target along the direction of the beam (0°). Pulse-shape discrimination was used to separate neutrons from γ-rays, and a time-of-flight spectrum was produced, showing the neutrons from the ^{3}H(d,n) reaction. These monitors were used as a check on the reliability of the charge integration by comparing the counts in the monitor with the charge collected in each run. The neutron monitor was also used to check for possible depolarization of the beam in the degrading foil and target. This will be discussed in section 2.7) of this chapter.

Figure 2-4: NaI detector system. The target chamber set-up shown here was used in obtaining the 8.6 MeV data.

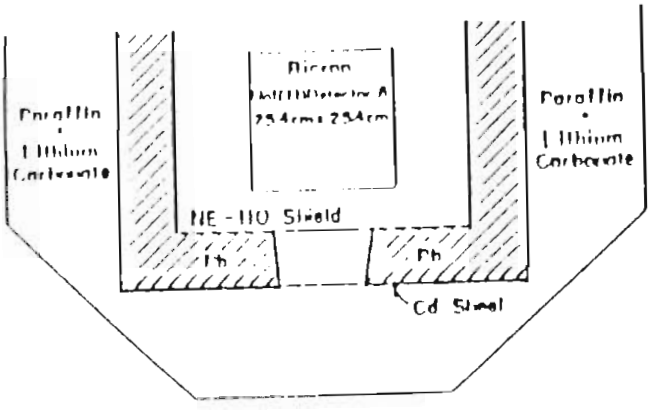
Paraffin
•
Lithium
Carbonate
NE-110 Shield
Pb
Pb
Cd Sheet
Paraffin
•
Lithium
Carbonate

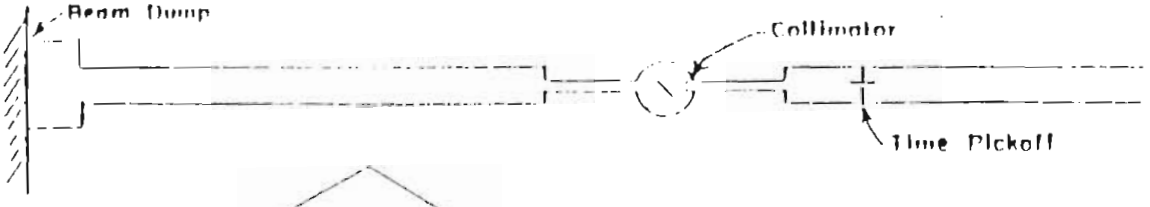
Beam Dump
Collimator
Time Pickoff

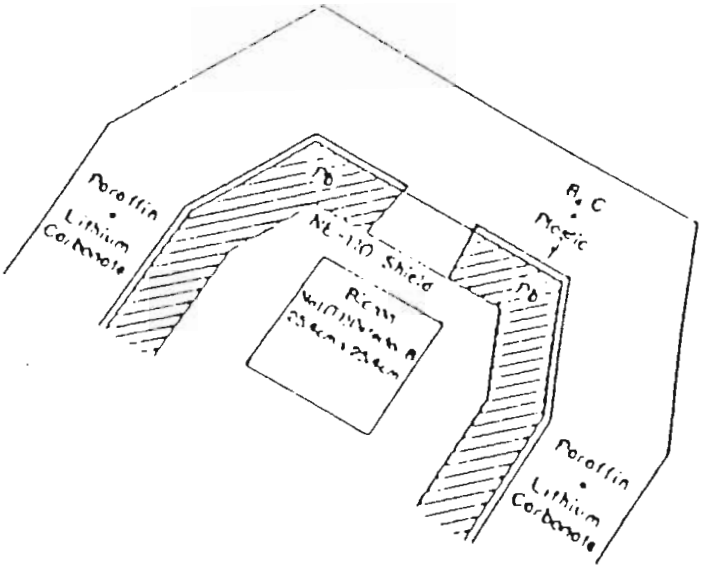
Paraffin
•
Lithium
Carbonate
Pb
NE-110 Shield
B4C
•
Plastic
Pb
Paraffin
•
Lithium
Carbonate

2.5) Targets

The targets used in this experiment were tritiated titanium foils manufactured at Oak Ridge National Laboratory. The tritium was deposited one for one with the titanium atoms in the foil while the foil was heated. The target used in the experiments at 8.6 MeV had a tritium thickness of 240 $\mu g/cm^2$ [Feldman, 1989]. The tritium thickness was obtained by comparing a measured elastic scattering cross section to the known value [Brolley, 1960]. The target was monitored by a solid-state detector for possible loss of tritium due to beam heating, and no effect was observed. The target used in the low energy experiments was approximately four times thicker. Subtraction of the background resulting from the titanium will be discussed in the next chapter.

2.6) Electronics

A schematic diagram of the electronics used in this experiment is shown in Figure 2-5. Light from events in the NaI were collected by six gain matched RCA 8575 photomultiplier tubes. The outputs of these tubes were mixed to form one signal which was clipped to 350 ns by a partially terminated coaxial cable of appropriate length. This signal was fanned out to a fast linear gate and a TD101 differential discriminator. The discriminator outputs were used for timing information (from a lower gate) and energy discrimination. The signal for energy discrimination was passed through a gate generator which held the fast linear gate open for 400 ns and then closed for 10 μs to reduce signal pileup from the NaI detector.

Figure 2-5:Electronics used in $^{3}H(d,\gamma)^{5}He$ experiment.

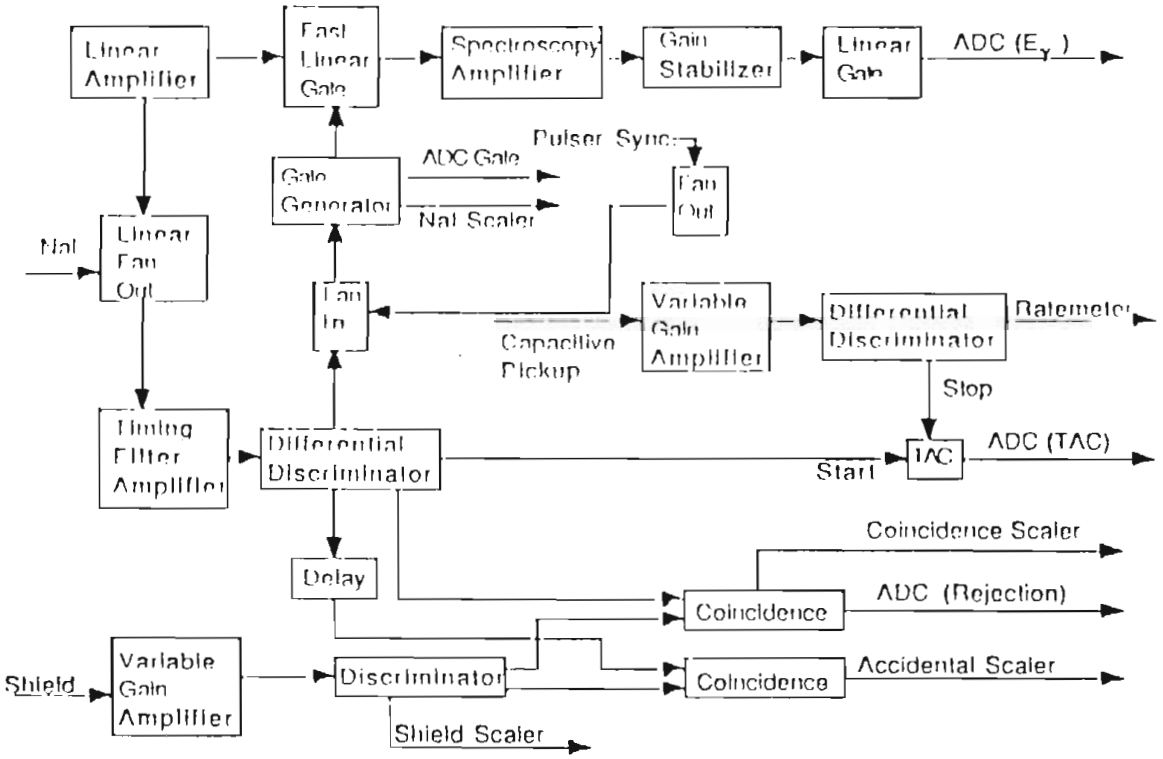
Linear Amplifier
Fast Linear Gate
Spectroscopy Amplifier
Gain Stabilizer
Linear Gate
ADC (E_γ)
Pulser Sync
ADC Gate
Gate Generator
NaI Scaler
Fan Out
NaI
Linear Fan Out
Fan In
Capacitive Pickup
Variable Gain Amplifier
Differential Discriminator
Ratemeter
Stop
Timing Filter Amplifier
Differential Discriminator
Start
TAC
ADC (TAC)
Coincidence Scaler
Delay
Coincidence
ADC (Rejection)
Shield
Variable Gain Amplifier
Discriminator
Coincidence
Accidental Scaler
Shield Scaler

The signal was then amplified and passed through a gain stabilizer. The gain stabilizer monitored an LED pulser in the NaI, compensating for any gain shifts that occurred. This LED was subsequently gated out by a linear gate before the signal was sent to an ADC, in order to avoid dead time which it might cause in the computer.

Signals from the plastic shield surrounding the NaI were sent through a variable gain amplifier and a fast discriminator. The output of the discriminator was sent to a coincidence box along with the output of the NaI differential discriminator. Signals from both within 60 ns of one another cause a coincidence output to be generated. This signal was sent to an ADC and used for software sorting of the NaI signal into accepted and rejected spectra. Cosmic rays and events not depositing their full energy into the NaI were removed using this technique. A second coincidence circuit was set up, identical to the first except that the NaI differential discriminator signal was delayed by 330 ns, allowing us to correct for accidental coincidences, which varied from 1% to 12%.

A high neutron production cross section exists in the d-^{3}H reaction, especially at forward angles at 8.6 MeV and isotropically at the lower energies used, necessitating the use of a time-of-flight (TOF) discrimination to remove the neutrons from the γ-ray spectrum. The output of the NaI differential discriminator was used to start a time-to-amplitude converter (TAC) which was stopped by a signal from the capacitive pickoff placed before the target chamber. The output from the TAC was sent to an ADC. The resulting spectrum showed a clear separation in time of the neutron and γ-ray events in the NaI. A logical gate set around the γ-ray peak was used in the software sorting of the NaI energy signal to give a spectrum corresponding to γ-rays in

the NaI. Using this TOF requirement allowed us to discriminate between γ-ray and neutron events in the NaI, as well as to reduce background that is uncorrelated in time. A typical spectrum for the NaI-TOF-TAC and the resulting NaI spectrum after background subtraction are shown in figures 2-6 and 2-7 respectively.

2.7) Measurement of deuteron energy at 400 keV.

The energy of the degraded deuteron beam was measured by scattering it off a thin (10 mg/cm^2) carbon foil and measuring the energy of the scattered particles with a calibrated silicon surface barrier detector of 100 micron thickness. The calibration was performed by elastically scattering deuterons of known energy off of the carbon foil at several energies. The measurement of the energy of the degraded beam was done starting with an incident deuteron beam of 4 MeV and lowering the energy until an optimum of beam transmission through the degrading foil, energy loss in the degrading foil, and resolution in beam energy of the resulting beam was reached. This optimum was a subjective judgement that we were as close to the fusion resonance region as possible while maintaining a decent current for count rate purposes and having reasonable definition of the energy of the beam. An energy spectrum from the silicon detector is shown in Figure 2-8. This corresponds to the conditions used for the experiment: the incident beam had an energy of 3.375 MeV before passing through Havar foils having a thickness of 1 mil (0.001"). There was a concern that depolarization of the deuteron beam might occur during the energy degrading and stopping in the target, so a

Figure 2-6:TAC spectrum. The left peak is the n's, and the right is the γ-rays. The time resolution of the γ-ray peak is 5 ns.

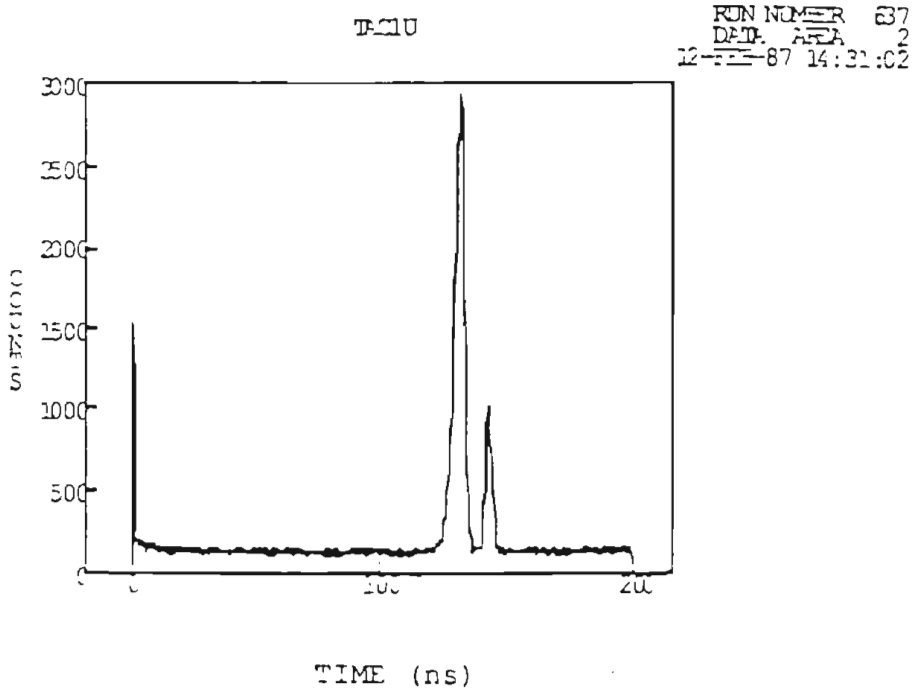
RUN NUMBER 87
12-FEB-87 14:31:02
2500
2000
1500
1000
500
0
TIME (ns)

Figure 2-7:Energy spectrum for the NaI detector after background subtraction.

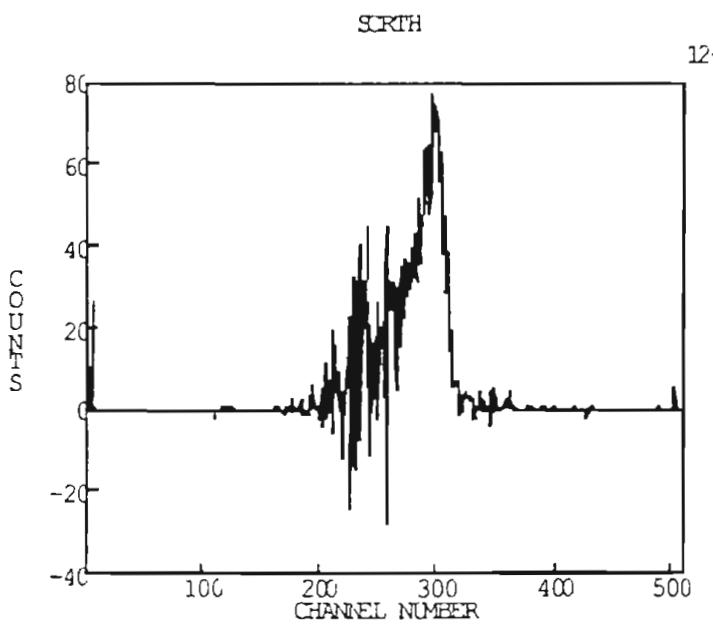
SORTH
RUN NUMBER 637
DATA AREA 196
12-FEB-87 14:21:19
COUNTS
80
60
40
20
0
-20
-40
100
200
300
400
500
CHANNEL NUMBER

Figure 2-8:Solid state detector spectrum of deuteron energy after the degrading foil.

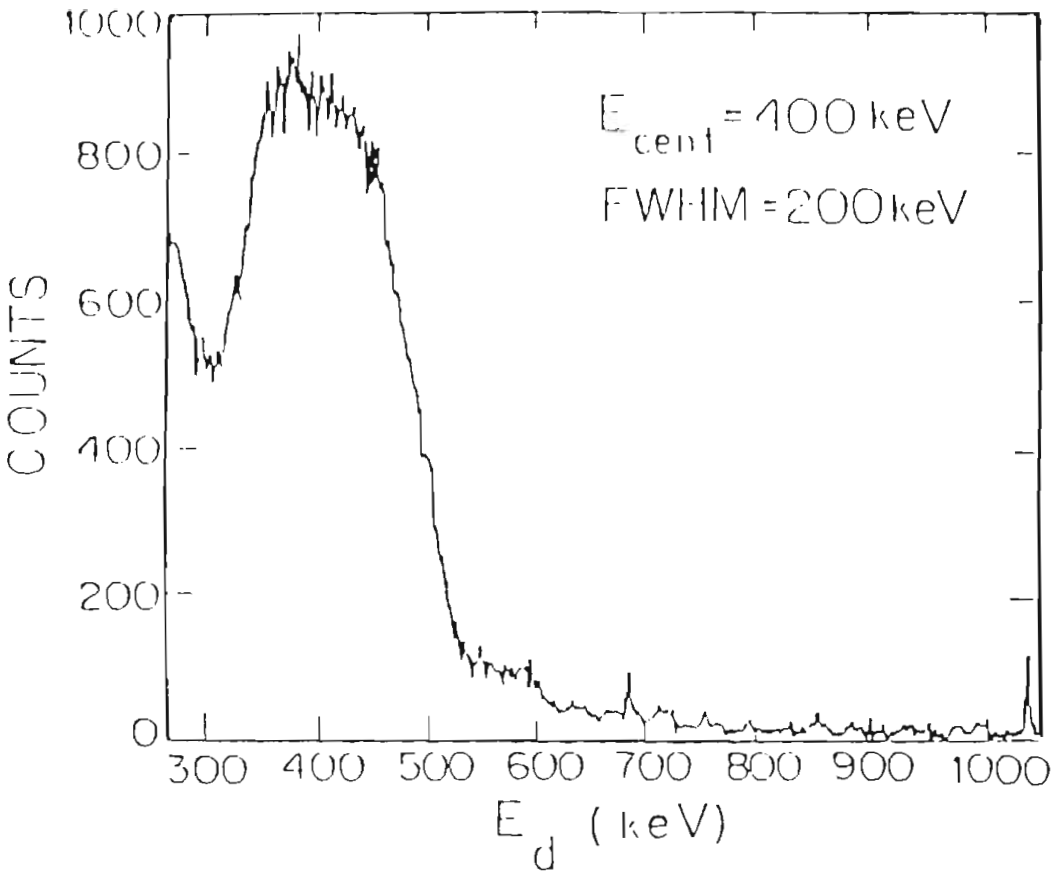
1000
800
600
400
200
0
COUNTS
300 400 500 600 700 800 900 1000
E d (keV)
E cent = 400 keV
FWHM = 200 keV

measurement of the polarization of the beam was performed via the known analyzing power of the $^{3}H(d,n)^{4}He$ reaction [Ohlsen, 1971; Grunder, 1971]. This was achieved by measuring the polarization at the energy used in the experiment, then lowering the incident deuteron energy in 20 keV steps and remeasuring the polarization until neutron production in the target ceased. No depolarization effects were observed. The results of this measurement are shown in Figure 2-9.

Figure 2-9:Polarization of the deuteron beam after degrading. The horizontal axis is the energy of the deuterons before the degrading foil. The circles represent measurements made using the m=1 and m=0 states of the deuteron. The crosses represent measurements made using the m=0 and m=-1 states of the deuteron.

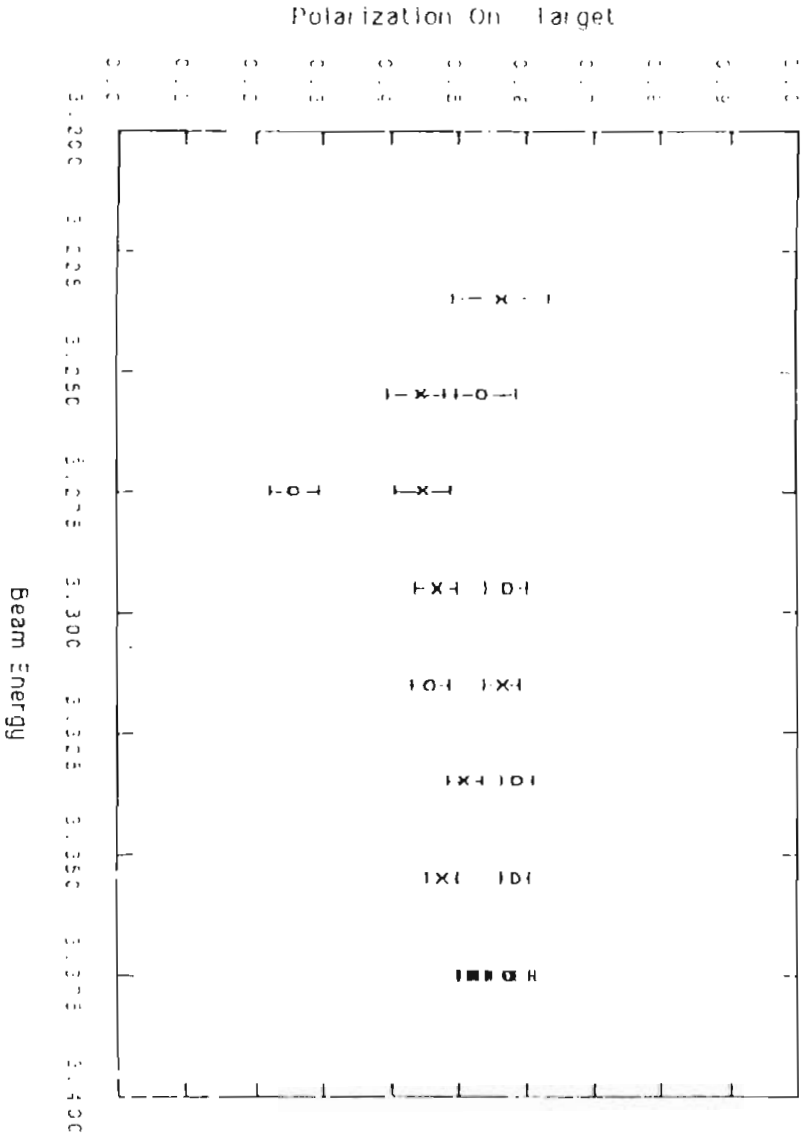
Polarization On Target
Beam Energy

CHAPTER 3

DATA REDUCTION

3.1 Fitting and summing procedures.

a) Background measurement and normalization

This experiment was performed using a tritiated titanium foil, necessitating measurement of the background resulting from the titanium so that it could be subtracted from the data. This was done by inserting a plain titanium foil of similar thickness to the tritiated titanium foil into the deuteron beam and counting with the NaI detectors, usually for 40% of the integrated charge (to obtain adequate statistical accuracy in the minimum time) used with the tritiated titanium foil. Corrections were made for the difference in integrated charge and for the slight difference in titanium foil thickness (note that the beam was stopped in the foil in the experiment at 400 keV, so that the thickness of the foreground and background foils was essentially equal.) The difference in thicknesses was measured by elastically scattering deuterons off of the titanium foils and collecting them in a solid-state silicon detector. The relative count rates, normalized by the total charge delivered to the target gave the ratio of the two titanium target thicknesses.

b) Summing Procedures

The summing of the γ-rays in the spectra was performed by the program Mulfit [King,1983], which fits the peak of interest to an empirically determined γ-ray response [Turner, 1978] ,determining the centroid and the FWHM width of the peak. The program sums 1.1 widths up from the centroid of the peak and a variable number of widths below

the centroid. In the experiment measuring $\sigma(\theta)$ and $A_y(\theta)$ at 8.6 MeV, the sum was carried out to 2.0 widths below the centroid. In the experiments measuring $T_{20}(\theta)$ at 8.6 MeV, the sum was done down to 1.0 widths below the centroid. For all of the experiments at E_d = 400 keV, the summing region was cut off at 0.5 widths below the centroid. The reason for summing less than 2 widths below the centroid in the above was to avoid background that was close to the γ-ray of interest. In the data at low energy, this was particulary a problem because of the large isotropic neutron flux.

3.2 Scaler Corrections

Several scalers were used for the purpose of correcting the data. The dead time in the ADC was corrected for by counting the number of gates used on the linear γ-ray signal previous to the ADC in a scaler and comparing this number to the number of events digitized by the ADC and stored in the spectrum. This correction varied from less than 1% to about 3%.

Accidental coincidences between the NaI and its surrounding shield were corrected for by storing two scalers that counted the number of real coincidences and the number of accidental coincidences. These numbers were used to correct the observed data by the factor

$$\frac{\text{COINCIDENCES}}{\text{COINCIDENCES-ACCIDENTALS}} \qquad 3\text{-}1$$

to get the actual number of counts that would have been seen in the absence of accidental coincidences. This correction dominated the correction factor used by the program Mulfit. This correction ranged between 2% and 15% with a typical value of 6% under normal conditions. An effort was made to hold this correction under 10% at all

times, but, occasionally, this was impossible because of the amount of beam needed to have the capacitive pickoff unit for TOF measurements function properly.

A correction for missed pickoffs in the TOF system was also made by counting the number of pickoffs and the amount of live time in the run with scalers. The number of pickoffs was compared to the frequency of the beam bunching multiplied by the time scaler to get the correction factor. This correction was generally held to 1% or less.

3.3 Corrected Data

The net sums of the γ-ray peak after background subtraction and corrections discussed in this chapter are presented in tables at the end of this section. Along with the corrected sums, the background sum, the correction factors for the foreground and background sums, and the BCI (integrated current) scaler for the foreground and background are presented. In subsequent calculations, the sums at 90 degrees have been corrected for the difference in target thickness caused by rotating the target so that it was not edge-on to the detector.

Table 3-1:Corrected sums from the $\sigma(\theta)$ and $A_y(\theta)$ measurements at 8.6 MeV. The columns from left to right are:1) laboratory angles of the right and left detectors;2)the run number;3)detector (right or left);4)spin state (up or down);5)beam current integrated with target foil in;6)beam current integrated with background foil in;7)correction factor used on data sum;8)correction factor used on background;9)data sum after corrections and background subtraction;10)background that was subtracted.

TABLE 3-1

LAB ANGLE	RUN	R/L	U/D	BCI FORE	BCI BACK	F1	F2	SUM	BACKGROUND
60° L 60° R									
	R0637	R	U	400.00	160.00	1.0545	1.0504	2626.74	1954.34
	R0637	L	U	400.00	160.00	1.0655	1.0611	2802.17	1567.19
	R0637	R	D	400.00	160.00	1.0589	1.0504	2956.92	1934.50
	R0637	L	D	400.00	160.00	1.0639	1.0611	2550.63	1633.08
137.5°L 42.5° R									
	R0643	R	U	400.00	160.00	1.0683	1.0661	2679.62	1892.59
	R0643	L	U	400.00	160.00	1.0419	1.0450	1749.46	2015.50
	R0643	R	D	400.00	160.00	1.0738	1.0661	2981.92	1893.51
	R0643	L	D	400.00	160.00	1.0424	1.0450	1873.06	1980.81
42.5°L 137.5°R									
	R0649	R	U	400.00	160.00	1.0376	1.0361	2017.46	1722.51
	R0649	L	U	400.00	160.00	1.0865	1.0843	2598.48	1694.48
	R0649	R	D	400.00	160.00	1.0367	1.0361	1886.67	1689.07
	R0649	L	D	400.00	160.00	1.0835	1.0843	2436.31	1733.16
130° L 130° R									
	R2613	R	U	400.00	160.00	1.0610	1.0566	2306.75	1770.82
	R2613	L	U	400.00	160.00	1.0588	1.0566	2128.16	2012.46
	R2613	R	D	400.00	160.00	1.0588	1.0566	2238.18	1803.06
	R2613	L	D	400.00	160.00	1.0456	1.0460	2084.57	1993.03
110° L 110° R									
	R2619	R	U	400.00	160.00	1.0564	1.0582	2643.48	1807.69
	R2619	L	U	400.00	160.00	1.0417	1.0442	2266.09	1914.46
	R2619	R	D	400.00	160.00	1.0556	1.0582	2419.82	1822.15
	R2619	L	D	400.00	160.00	1.0416	1.0442	2364.50	1865.86
90° L 90° R									
	R2625	R	U	400.00	160.00	1.0677	1.0429	3352.68	2249.67
	R2625	L	U	400.00	160.00	1.0463	1.0501	2861.79	2170.17

	R2625	R	D	400.00	160.00	1.0686	1.0429	3357.02	2232.60
	R2625	L	D	400.00	160.00	1.0468	1.0501	2967.83	2168.19
70° L 70° R									
	R2631	R	U	400.00	160.00	1.0610	1.0494	3053.01	1824.87
	R2631	L	U	400.00	160.00	1.0428	1.0559	2475.66	1834.45
	R2631	R	D	400.00	160.00	1.0588	1.0494	2983.46	1774.39
	R2631	L	D	400.00	160.00	1.0456	1.0559	2355.60	1817.19

Table 3-2:Corrected sums from the $T_{20}(\theta)$ measurements at 8.6 MeV. The columns from left to right are:1) laboratory angles of the right and left detectors;2)the run number;3)detector (right or left);4)spin state (m=1 or 2);5)beam current integrated with target foil in;6)beam current integrated with background foil in;7)correction factor used on data sum;8)correction factor used on background;9)data sum after corrections and background subtraction;10)background that was subtracted.

TABLE 3-2

LAB ANGLE	RUN	R/L	STATE	BCI	BCI	F1	F2	SUM	BACKGROUND
90° L									
90° R									
	R0813	R	1	151.23	117.30	1.1009	1.1361	793.97	151.10
	R0813	L	1	151.23	117.30	1.0858	1.1204	807.63	214.42
	R0813	R	2	148.77	122.70	1.0993	1.1212	804.65	139.51
	R0813	L	2	148.77	122.70	1.0860	1.1033	800.05	187.28
130° L									
130° R									
	R0842	R	1	225.20	90.38	1.0545	1.0672	689.18	170.45
	R0842	L	1	225.20	90.38	1.0480	1.0614	668.11	244.48
	R0842	R	2	224.80	89.62	1.0555	1.0534	716.51	185.83
	R0842	L	2	224.80	89.62	1.0479	1.0490	676.98	283.44
70° L									
70° R									
	R0845	R	1	249.60	100.85	1.0756	1.0693	1280.50	172.19
	R0845	L	1	249.60	100.85	1.0595	1.0563	1274.76	266.03
	R0845	R	2	250.40	99.15	1.0774	1.0675	1327.74	148.78
	R0845	L	2	250.40	99.15	1.0595	1.0556	1301.47	255.74
50° L									
50° R									
	R0848	R	1	174.84	70.43	1.1130	1.0894	1148.33	129.28
	R0848	L	1	174.84	70.43	1.0820	1.0758	1244.71	170.34
	R0848	R	2	175.16	69.57	1.1173	1.0919	1249.45	94.38
	R0848	L	2	175.16	69.57	1.0825	1.0752	1295.10	156.30
130° L									
130° R									
	R2803	R	1	149.18	119.34	1.0803	1.0784	468.02	96.81
	R2803	L	1	149.18	119.34	1.0681	1.0685	416.30	156.50
	R2803	R	2	150.81	120.66	1.0775	1.0749	447.89	139.96
	R2803	L	2	150.81	120.66	1.0640	1.0664	440.34	161.11
110° L									
110° R									
	R2810	R	1	299.27	119.51	1.0781	1.0889	1082.14	244.45
	R2810	L	1	299.27	119.51	1.0671	1.0754	1139.58	349.77

	R2810	R	2	300.73	120.49	1.0774	1.0888	1065.69	301.98
	R2810	L	2	300.73	120.49	1.0660	1.0740	1266.91	295.09
137.5° L 42.5° R									
	R2838	R	1	225.79	119.39	1.1334	1.1063	1360.73	153.47
	R2838	L	1	225.79	119.39	1.0473	1.0439	680.09	257.69
	R2838	R	2	224.21	120.63	1.1407	1.1056	1472.11	130.45
	R2838	L	2	224.21	120.63	1.0472	1.0449	676.18	249.31

Table 3-3:Corrected sums from the differential cross section measurements at 400 keV. The columns from left to right are:1) run number 2)laboratory angles of the right and left detectors;3)detector (right or left);4)beam current integrated with target foil in;5)correction factor used on data sum;6)correction factor used on background;7)data sum after corrections and background subtraction;8)background that was subtracted;9)the ratio of the target foil BCI to the background foil BCI.

TABLE 3-3

RUN	θ	R/L	BCI	F1	F2	SUM	BKGND	FORE/BACK BCI RATIO
R1000	130	R	450.00	1.1813	1.0432	2947.44	487.63	2.5
R1000	130	L	450.00	1.1236	1.0353	2198.15	354.70	2.5
R1002	110	R	450.04	1.1765	1.0393	2798.61	506.10	2.5
R1002	110	L	450.04	1.1127	1.0314	2035.38	388.58	2.5
R1004	90	R	450.00	1.1504	1.0349	2763.60	483.04	2.5
R1004	90	L	450.00	1.1004	1.0291	2293.33	392.80	2.5
R1006	70	R	450.00	1.1923	1.0337	2877.57	386.93	2.5
R1006	70	L	450.00	1.1299	1.0301	2098.77	369.99	2.5
R1008	50	R	450.00	1.1724	1.0347	2897.01	383.72	2.5
R1008	50	L	450.00	1.1183	1.0298	2377.58	321.18	2.5
R1010	138.3	R	450.00	1.1667	1.0706	2928.87	550.31	2.5
R1010	30	L	450.00	1.1237	1.0298	2510.47	386.25	2.5
R1012	37.8	R	450.00	1.1815	1.0348	3010.04	506.85	2.5
R1012	135	L	450.00	1.1109	1.0319	2462.86	409.25	2.5
R1014	130	R	450.00	1.1503	1.0340	2811.02	409.80	2.5
R1014	130	L	450.00	1.1108	1.0291	2450.16	416.41	2.5
R1016	110	R	450.00	1.1735	1.0351	3061.57	387.48	2.5
R1016	110	L	450.00	1.1213	1.0319	2558.53	338.15	2.5
R1018	90	R	450.00	1.1926	1.0379	3170.58	423.65	2.5
R1018	90	L	450.00	1.1424	1.0341	2707.74	304.86	2.5

Table 3-4:Corrected sums from the $A_y(\theta)$ and $A_{yy}(\theta)$ measurements at 400 keV. The columns from left to right are:1) laboratory angles of the right and left detectors;2)the run number;3)spin state (state m=1,2,or3)(up or down);4)detector (right or left);5)beam current integrated with target foil in;6)correction factor used on data sum;7)correction factor used on background;8)data sum after corrections and background subtraction;9)background that was subtracted;10)ratio of target foil BCI to background foil BCI.

TABLE 3-4

LAB ANGLE	RUN	STATE	R/L	BCI	F1	F2	SUM	BKGND	FORE/BACK BCI
110° L									
110° R									
	R1041	1U	R	675.00	1.0611	1.0205	1241.70	246.00	2.5
	R1041	1U	L	675.00	1.0639	1.0172	1060.53	148.16	2.5
	R1042	2U	R	675.00	1.0651	1.0198	1138.28	211.50	2.5
	R1042	2U	L	675.00	1.0822	1.0190	971.95	225.13	2.5
	R1043	3U	R	675.00	1.0550	1.0188	1315.46	252.61	2.5
	R1043	3U	L	675.00	1.0804	1.0187	1115.78	159.18	2.5
	R1044	2U	R	675.00	1.0191	1.0198	1082.09	240.94	2.5
	R1044	2U	L	675.00	1.0474	1.0190	960.26	239.24	2.5
	R1045	1D	R	675.00	1.0199	1.0169	1219.25	231.29	2.5
	R1045	1D	L	675.00	1.0557	1.0196	972.38	238.65	2.5
	R1046	2D	R	675.00	1.0298	1.0198	1096.23	205.93	2.5
	R1046	2D	L	675.00	1.0488	1.0190	882.89	229.94	2.5
	R1047	3D	R	675.00	1.0888	1.0200	1163.24	184.17	2.5
	R1047	3D	L	675.00	1.0939	1.0216	1041.30	183.07	2.5
	R1048	2D	R	675.00	1.0587	1.0198	1165.50	238.92	2.5
	R1048	2D	L	675.00	1.0566	1.0190	926.03	208.19	2.5
130° L									
130° R									
	R1101	1D	R	400.00	1.1498	1.0955	1693.12	284.72	5.
	R1101	1D	L	400.00	1.0987	1.0844	1730.45	249.41	5.
	R1102	2D	R	200.00	1.0662	1.0566	822.16	105.45	2.5
	R1102	2D	L	200.00	1.0595	1.0457	817.68	143.78	2.5
	R1103	3D	R	200.00	1.1172	1.0482	877.39	107.75	1.
	R1103	3D	L	200.00	1.0718	1.0405	896.09	144.63	1.
	R1105	2D	R	200.00	1.1013	1.0566	815.10	105.45	2.5
	R1105	2D	L	200.00	1.0666	1.0457	785.71	143.78	2.5
	R1106	1U	R	200.00	1.1267	1.0482	858.44	107.75	1.
	R1106	1U	L	200.00	1.0894	1.0405	821.67	144.63	1.
	R1107	2U	R	200.00	1.1276	1.0566	862.91	105.45	2.5
	R1107	2U	L	200.00	1.1024	1.0457	791.46	143.78	2.5
	R1108	3U	R	200.00	1.1087	1.0955	855.05	142.36	2.5
	R1108	3U	L	200.00	1.0721	1.0844	846.66	124.71	2.5
	R1109	2U	R	200.00	1.0958	1.0566	858.95	105.45	2.5

	R1109	2U	L	200.00	1.0701	1.0457	791.96	143.78	2.5
90° L									
90° R									
	R1113	3U	R	200.00	1.1075	1.1997	852.79	104.73	2.5
	R1113	3U	L	200.00	1.0722	1.1900	799.07	148.75	2.5
	R1114	2U	R	200.00	1.0962	1.0637	687.42	135.41	2.5
	R1114	2U	L	200.00	1.0680	1.0555	740.68	137.22	2.5
	R1115	1U	R	200.00	1.1074	1.0639	767.24	138.31	2.5
	R1115	1U	L	200.00	1.0717	1.0528	777.50	121.07	2.5
	R1116	2U	R	200.00	1.0906	1.0637	747.58	135.41	2.5
	R1116	2U	L	200.00	1.0661	1.0555	730.59	137.22	2.5
	R1117	2D	R	200.00	1.1064	1.0637	761.48	135.41	2.5
	R1117	2D	L	200.00	1.0753	1.0555	809.05	137.22	2.5
	R1118	3D	R	200.00	1.1075	1.0639	785.90	138.31	2.5
	R1118	3D	L	200.00	1.0707	1.0528	790.58	121.07	2.5
	R1119	1D	R	200.00	1.1216	1.1997	799.86	104.73	2.5
	R1119	1D	L	200.00	1.0918	1.1900	678.83	148.75	2.5
	R1120	2D	R	200.00	1.1002	1.0637	787.28	135.41	2.5
	R1120	2D	L	200.00	1.0782	1.0555	791.12	137.22	2.5
70° L									
70° R									
	R1124	1D	R	200.00	1.1243	1.0509	893.55	139.14	2.5
	R1124	1D	L	200.00	1.0906	1.0404	818.01	148.26	2.5
	R1125	2D	R	200.00	1.0804	1.0457	830.68	104.36	2.5
	R1125	2D	L	200.00	1.0532	1.0347	852.36	108.64	2.5
	R1126	3D	R	200.00	1.1241	1.0390	878.33	111.48	2.5
	R1126	3D	L	200.00	1.0858	1.0312	898.81	121.17	2.5
	R1127	2D	R	200.00	1.1058	1.0457	903.55	104.36	2.5
	R1127	2D	L	200.00	1.0761	1.0347	821.54	108.64	2.5
	R1128	2U	R	200.00	1.0917	1.0457	831.95	104.36	2.5
	R1128	2U	L	200.00	1.0674	1.0347	866.34	108.64	2.5
	R1129	1U	R	200.00	1.1289	1.0390	858.90	111.48	2.5
	R1129	1U	L	200.00	1.0924	1.0312	870.03	121.17	2.5
	R1130	2U	R	200.00	1.1049	1.0457	919.44	104.36	2.5
	R1130	2U	L	200.00	1.0708	1.0347	863.02	108.64	2.5
	R1131	3U	R	200.00	1.1267	1.0509	930.24	141.77	2.5
	R1131	3U	L	200.00	1.0839	1.0404	832.67	148.26	2.5
50° L									

50° R									
	R1135	1U	R	200.00	1.1218	1.0429	1038.07	122.44	2.5
	R1135	1U	L	200.00	1.0809	1.0337	990.08	105.95	2.5
	R1136	2U	R	200.00	1.0940	1.0437	863.62	109.43	2.5
	R1136	2U	L	200.00	1.0666	1.0347	901.88	106.06	2.5
	R1137	3U	R	200.00	1.1752	1.0364	1008.38	121.67	2.5
	R1137	3U	L	200.00	1.1327	1.0313	973.13	110.86	2.5
	R1138	2U	R	200.00	1.1022	1.0437	896.41	109.43	2.5
	R1138	2U	L	200.00	1.0743	1.0347	996.18	106.06	2.5
	R1139	2D	R	200.00	1.1285	1.0437	1157.38	109.43	2.5
	R1139	2D	L	200.00	1.0921	1.0347	1266.71	106.06	2.5
	R1140	3D	R	200.00	1.1558	1.0429	1337.64	122.44	2.5
	R1140	3D	L	200.00	1.1029	1.0337	1349.87	105.95	2.5
	R1141	1D	R	200.00	1.1692	1.0364	1219.70	121.67	2.5
	R1141	1D	L	200.00	1.1181	1.0313	1320.30	110.86	2.5
	R1142	2D	R	200.00	1.1089	1.0437	1003.33	109.43	2.5
	R1142	2D	L	200.00	1.0749	1.0347	1003.24	106.06	2.5
42.5° L									
137.5°R									
	R1146	1D	R	200.00	1.1104	1.0510	861.27	115.50	2.5
	R1146	1D	L	200.00	1.0839	1.0449	1170.51	128.00	2.5
	R1147	2D	R	200.00	1.0895	1.0668	851.34	85.13	2.5
	R1147	2D	L	200.00	1.0700	1.0574	1118.97	116.31	2.5
	R1148	3D	R	200.00	1.1249	1.0634	865.71	103.58	2.5
	R1148	3D	L	200.00	1.1006	1.0558	1012.89	166.29	2.5
	R1150	2D	R	200.00	1.0894	1.0668	838.44	85.13	2.5
	R1150	2D	L	200.00	1.0707	1.0574	975.23	116.31	2.5
	R1151	2U	R	200.00	1.0854	1.0668	854.35	85.13	2.5
	R1151	2U	L	200.00	1.0659	1.0574	903.20	116.31	2.5
	R1152	3U	R	200.00	1.1052	1.0510	918.61	115.50	2.5
	R1152	3U	L	200.00	1.0811	1.0449	1129.32	128.00	2.5
	R1153	1U	R	200.00	1.1212	1.0634	1037.02	103.58	2.5
	R1153	1U	L	200.00	1.0960	1.0558	1454.05	166.29	2.5
	R1154	2U	R	200.00	1.1242	1.0668	862.10	85.13	2.5
	R1154	2U	L	200.00	1.1067	1.0574	1002.99	116.31	2.5
110° L									
110° R									
	R1158	3U	R	200.00	1.1268	1.0410	970.28	106.60	2.5

	R1158	3U	L	200.00	1.0831	1.0334	900.36	118.84	2.5
	R1159	2U	R	200.00	1.0943	1.0423	892.05	111.84	2.5
	R1159	2U	L	200.00	1.0660	1.0342	867.57	116.35	2.5
	R1160	1U	R	200.00	1.1182	1.0463	960.75	128.07	2.5
	R1160	1U	L	200.00	1.0813	1.0365	862.27	176.20	2.5
	R1161	2U	R	200.00	1.1097	1.0423	720.04	111.84	2.5
	R1161	2U	L	200.00	1.0855	1.0342	769.42	121.52	2.5
90° L									
90° R									
	R1218	1U	R	250.00	1.0751	1.0367	1224.53	103.02	2.
	R1218	1U	L	250.00	1.0559	1.0362	1314.06	151.95	2.
	R1219	2U	R	250.00	1.0560	1.0376	1021.43	103.14	2.
	R1219	2U	L	250.00	1.0470	1.0381	1366.86	144.57	2.
	R1220	3U	R	250.00	1.0634	1.0372	1136.41	124.49	2.
	R1220	3U	L	250.00	1.0497	1.0380	1214.26	84.65	2.
	R1221	2U	R	250.00	1.0629	1.0376	984.53	102.70	2.
	R1221	2U	L	250.00	1.0500	1.0381	926.15	86.46	2.
	R1222	2D	R	250.00	1.0646	1.0376	1143.50	100.38	2.
	R1222	2D	L	250.00	1.0506	1.0381	903.95	80.97	2.
	R1223	3D	R	250.00	1.0753	1.0367	1375.31	102.49	2.
	R1223	3D	L	250.00	1.0575	1.0362	1258.93	107.97	2.
	R1224	2D	R	250.00	1.0618	1.0376	1010.86	101.30	2.
	R1224	2D	L	250.00	1.0513	1.0381	923.73	75.93	2.
	R1225	1D	R	250.00	1.0725	1.0372	1419.38	118.57	2.
	R1225	1D	L	250.00	1.0555	1.0380	1496.26	101.10	2.
70° L									
70° R									
	R1229	1U	R	250.00	1.0656	1.0372	1385.90	103.39	2.
	R1229	1U	L	250.00	1.0506	1.0347	1567.11	115.35	2.
	R1230	2U	R	250.00	1.0577	1.0354	1018.05	122.31	2.
	R1230	2U	L	250.00	1.0468	1.0372	903.84	89.20	2.
	R1231	3U	R	250.00	1.0670	1.0359	992.31	82.95	2.
	R1231	3U	L	250.00	1.0519	1.0372	1158.44	125.36	2.
	R1232	2U	R	250.00	1.0680	1.0354	903.34	112.55	2.
	R1232	2U	L	250.00	1.0497	1.0372	907.43	93.57	2.
	R1233	2D	R	250.00	1.0651	1.0354	1072.99	119.57	2.
	R1233	2D	L	250.00	1.0509	1.0372	1192.72	112.17	2.
	R1234	3D	R	250.00	1.0739	1.0372	1192.33	117.15	2.

	R1234	3D	L	250.00	1.0569	1.0347	1341.08	113.87	2.
	R1235	2D	R	250.00	1.0613	1.0354	1034.72	116.93	2.
	R1235	2D	L	250.00	1.0480	1.0372	1091.84	116.65	2.
	R1236	1D	R	250.00	1.0723	1.0359	1101.53	101.77	2.
	R1236	1D	L	250.00	1.0546	1.0372	1065.61	132.43	2.
℄30° L									
℄30° R									
	R1240	1D	R	250.00	1.0633	1.0373	780.45	156.12	2.5
	R1240	1D	L	250.00	1.0513	1.0343	746.91	147.39	2.
	R1241	1D	R	250.00	1.0666	1.0373	924.78	179.31	2.5
	R1241	1D	L	250.00	1.0549	1.0343	785.36	144.80	2.5
	R1242	2D	R	250.00	1.0549	1.0385	861.63	140.29	2.5
	R1242	2D	L	250.00	1.0472	1.0395	737.47	128.72	2.5
	R1243	3D	R	250.00	1.0702	1.0337	851.85	174.06	2.5
	R1243	3D	L	250.00	1.0560	1.0364	896.98	136.19	2.5
	R1244	2D	R	250.00	1.0559	1.0385	841.77	125.01	2.5
	R1244	2D	L	250.00	1.0494	1.0395	745.72	122.15	2.5
	R1245	1U	R	125.00	1.0701	1.0337	456.13	90.35	1.25
	R1245	1U	L	125.00	1.0582	1.0364	396.93	53.49	1.25
	R1246	2U	R	125.00	1.0554	1.0385	394.92	66.45	1.25
	R1246	2U	L	125.00	1.0473	1.0395	338.29	60.75	1.25
	R1247	3U	R	125.00	1.0711	1.0373	432.15	74.80	1.25
	R1247	3U	L	125.00	1.0597	1.0343	365.76	67.95	1.25
	R1248	2U	R	125.00	1.0620	1.0385	377.38	67.58	1.25
	R1248	2U	L	125.00	1.0530	1.0395	398.66	63.69	1.25

Chapter 4

Experimental Results

4.1 $\sigma(\theta)$, $A_y(\theta)$, and $T_{20}(\theta)$ at 8.6 MeV

The absolute cross section, as a function of angle and energy, is given by

$$\sigma(\theta,E) = \frac{N_\gamma(\theta,E)}{N_d N_t \Omega \varepsilon} \quad , \tag{4.1}$$

where N_γ is the number of counts of the γ-ray of interest in the detector, N_d is the number of deuterons incident on the target, N_t is the number of tritium nuclei/cm^2, Ω is the solid angle of the detector, and ε is the detector efficiency.

N_γ was determined by methods discussed in the previous chapter. In all of these experiments, Ω was 0.045 sr for the distance of 41.75 inches between the target and the rear face of the NaI detector. ε is defined as the ratio of the observed γ-rays, N_γ, to the actual number of γ-rays entering the detector. The method used to determine the efficiency has been previously published [Weller, 1980]. The efficiency of the right NaI in this experiment was 0.21 for a γ-ray energy of 22 MeV. The left NaI was normalized to the right.

Some systematic errors are involved in the absolute cross section. N_γ is estimated to have an uncertainty of 10% due to the choice of summing region. The product $\Omega\varepsilon$ is estimated to have an uncertainty of 10%. Due to non-uniformities in the target, and possible movement of the beam spot on target, N_t is estimated to have an uncertainty

of 10%. Checks on charge integration have indicated that an uncertainty of 1% is involved due to charge that did not enter the Faraday cup and drift in the charge integrator. Propagation of these uncertainties implies that the systematic error in the absolute cross section is on the order of 17%.

For a spin-one incident particle, the differential cross section is given by [Seyler and Weller,1979]

$$\sigma(\theta,\phi) = \sigma(\theta)[1 + \frac{3}{2} p_y A_y(\theta) + t_{20}T_{20}(\theta) + 2\mathrm{Re}t_{21}T_{21}(\theta) + 2\mathrm{Re}t_{22}T_{22}(\theta)]$$

4-2

Expansion in terms of Legendre and associated Legendre polynomials gives

$$\sigma(\theta,\phi) = A_0 \sum_{k=0}^{k=ax} [a_k P_k(\cos\theta) + b_k p_y P_k^1(\cos\theta) + c_k t_{20} P_k(\cos\theta) + d_k \mathrm{Re}t_{21} P_k^1(\cos\theta) + e_k \mathrm{Re}t_{22} P_k^2(\cos\theta)]$$

4-3

where the Legendre polynomials used are given by (using $x=\cos(\theta)$)

$$P_n(x) = \frac{1}{2^n n!} \frac{d^n}{dx^n}(x^2-1)^n \quad \text{,where } n=0,1,2...$$

4-4

and the associated Legendre polynomials are given by

$$P_n^m(x) = (1-x^2)^{m/2} \frac{d^m}{dx^m} P_n(x)$$

4-5

The following notation is used to define the coordinate system of this experiment:

4-6 $\mathbf{k}_{in}$ ≡ direction of propagation of incoming particle

$\mathbf{k}_{out}$ ≡ direction of propagation of outgoing particle

$\mathbf{y} \equiv \mathbf{k}_{in} \times \mathbf{k}_{out}$ (in a right-handed coordinate system)

$\mathbf{z} \equiv \mathbf{k}_{in}$

$\mathbf{s}$ ≡ polarization axis of the beam

β ≡ angle between $\mathbf{k}_{in}$ and $\mathbf{s}$

ϕ ≡ angle between the projection of $\mathbf{s}$ in the $\mathbf{y}$-$\mathbf{z}$ plane and the $\mathbf{y}$ axis ($\phi > 0$ towards + $\mathbf{x}$)

In this notation [Darden, 1970]:

$$P_y = P_z \sin\beta\cos\phi$$

$$t_{20} = \frac{P_{zz}}{2\sqrt{2}}(3\cos^2\beta - 1)$$

$$Ret_{21} = \frac{P_{zz}\sqrt{3}}{4} \sin 2\beta \sin\phi$$

$$Ret_{22} = \frac{-P_{zz}\sqrt{3}}{4} \sin^2\beta\cos 2\phi$$

for a deuteron beam, where P_z and P_{zz} are the vector and tensor polarizations, respectively.

For unpolarized beam, Equation 4-3 reduces to

$$\frac{\sigma(\theta)}{A_0} = 1 + \sum_{k=1} a_k Q_k P_k$$

4-7

where the factor Q_k has been introduced as a correction for the finite size of the detector.

In order to obtain the b_k coefficients of Equation 4-3, the polarized source is run in states where $P_{zz}=0$, $\beta=90°$, $\phi=0°$, and $P_z=+1$ for the state "+"; and $\phi=180°$, and $P_z=-1$ for the state "-". Taking Equation 4-3 for these cases and comparing with Equation 4-2, we obtain (noting that $P_y^+ = -P_y^- = P_y$)

$$\frac{\frac{3}{2}\sigma(\theta)A_y(\theta)}{A_0} = \sum_{k=1} b_k Q_k P_k^1 \ (\cos\theta)$$

4-8

and

$$A_y = \frac{2}{3}\,\frac{1}{P_y}\,\frac{\sigma^+ - \sigma^-}{\sigma^+ + \sigma^-}$$

.

The TUNL Lamb-Shift PIS produces a beam polarization of $P_y=-2Q/3$, where Q is the percentage beam polarization, when in this purely vector polarized deuteron mode.

Measuring the tensor analyzing power $T_{20}(\theta)$ allowed us to obtain the c_k coefficients of Equation 4-3 by running the source in the mode where $P_z\neq0$, $P_{zz}\neq0$, $\beta=0$, and ϕ is undetermined. In this mode $P_y=Ret_{21}=Ret_{22}=0$ and $t_{20}=P_{zz}/\sqrt{2}$. We will call the tensor moment of hyperfine state m=1 t_1 and that of state m=0 t_2. Taking Equation 4-3 for the source in this mode and in these two states, and comparing to Equation 4-2, we obtain:

$$\frac{T_{20}(\theta)\ \sigma(\theta)}{A_0} = \sum_{k=0} c_k Q_k P_k^1 (\cos\theta)\ ,$$

4-9

$$T_{20}(\theta) = \frac{\sigma_1 - \sigma_2}{\sigma_2 t_1 - \sigma_1 t_2}$$

and

.

If we note that the polarizations of t_1 ($P_{zz}=1$) and t_2 ($P_{zz}=-2$) make it convenient to express them as $t_{20}=-2t_1=t_2$ and that $t_{20}=-Q\sqrt{2}$, where Q is the percentage polarization of the beam, we can express $T_{20}(\theta)$ as

$$T_{20}(\theta) = \frac{\sqrt{2}}{Q}\,\frac{\sigma_1 - \sigma_2}{2\sigma_1 + \sigma_2}$$

4-10

.

Unpolarized differential cross section, vector analyzing power, and tensor analyzing power angular distributions were measured at seven angles at E_d=8.6 MeV and are shown in Figures 4-1, 4-2, and 4-3 respectively and given in Table 4-1. The polynomial fits described in

Equations 4-7, 4-8, and 4-9 are shown in Figures 4-4, 4-5, 4-6 respectively, and the coefficients derived are given in Table 4-2.

Figure 4-1:Absolute cross section at 8.6 MeV. $\sigma(\theta)$ is given in μb/sr. The error bars represent statistical uncertainties associated with the data points. The absolute cross section has an additional systematic error on the order of 17% (see text).

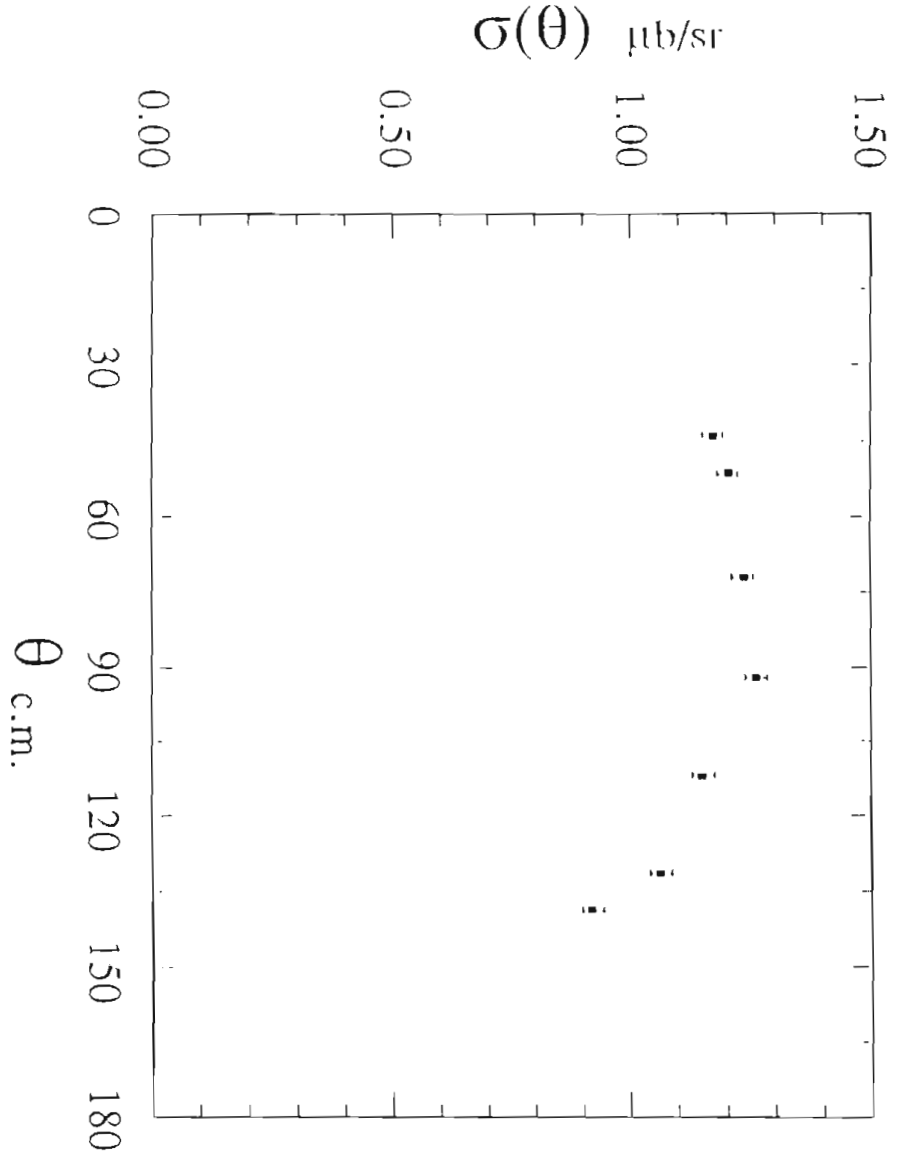
σ(θ) μb/sr
0.00
0.50
1.00
1.50
0
30
60
90
120
150
180
θ c.m.

Figure 4-2:Vector anayzing power $A_y(\theta)$ at 8.6 MeV. The error bars represent statistical uncertainties associated with the data points.

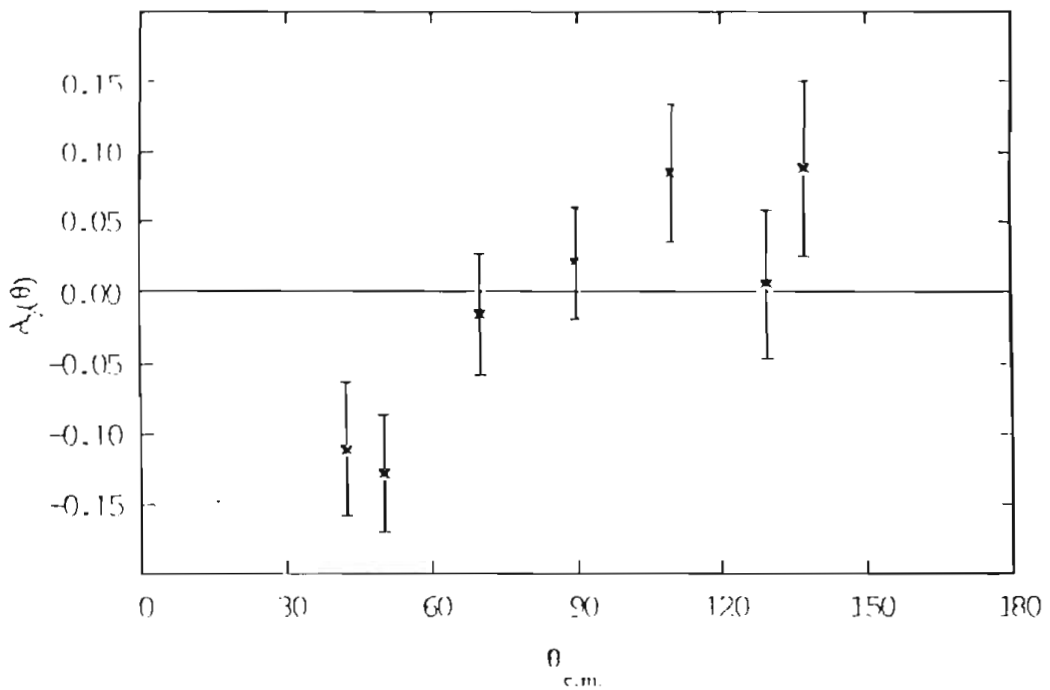
0.15
0.10
0.05
0.00
-0.05
-0.10
-0.15
$A_y(\theta)$
0
30
60
90
120
150
180
$\theta_{c.m.}$

Figure 4-3:Tensor analyzing power $T_{20}(\theta)$ at 8.6 MeV. The error bars represent statistical uncertainties associated with the data points.

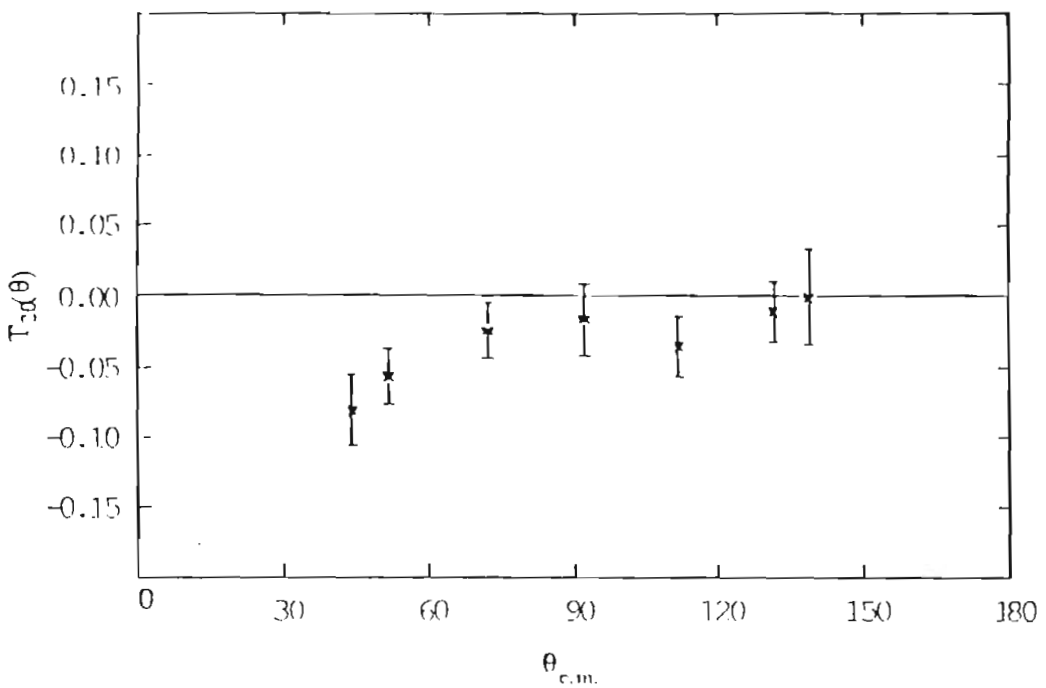
0.15
0.10
0.05
0.00
-0.05
-0.10
-0.15
$T_{2d}(\theta)$
0
30
60
90
120
150
180
$\theta_{c.m.}$

Table 4-1: $\sigma(\theta)$, $A_y(\theta)$, $T_{20}(\theta)$ at 8.6 MeV.

$\theta_{c.m.}$	$d\sigma/d\Omega$	ERROR $d\sigma/d\Omega$	$A_y(\theta)$	ERROR $A_y(\theta)$	$T_{20}(\theta)$	ERROR $T_{20}(\theta)$
	$\mu b/sr$	$\mu b/sr$				
44.005	1.17190	0.02186	-0.112	.047	-0.082	0.026
51.703	1.20315	0.02202	-0.129	.042	-0.058	0.020
72.077	1.23436	0.02215	-0.016	.043	-0.025	0.020
92.196	1.26145	0.02320	0.021	.040	-0.017	0.025
112.050	1.15255	0.02306	0.085	.050	-0.036	0.022
131.662	1.06383	0.02321	0.006	.053	-0.011	0.021
138.963	0.92058	0.02244	0.088	.063	-0.001	0.034

Figure 4-4:Legendre polynomial fit obtained using Equation 4-7 for $^{3}H(d,\gamma)^{5}He$ at 8.6 MeV. The error bars represent statistical uncertainties associated with the data points. The solid line is the fit to the data.

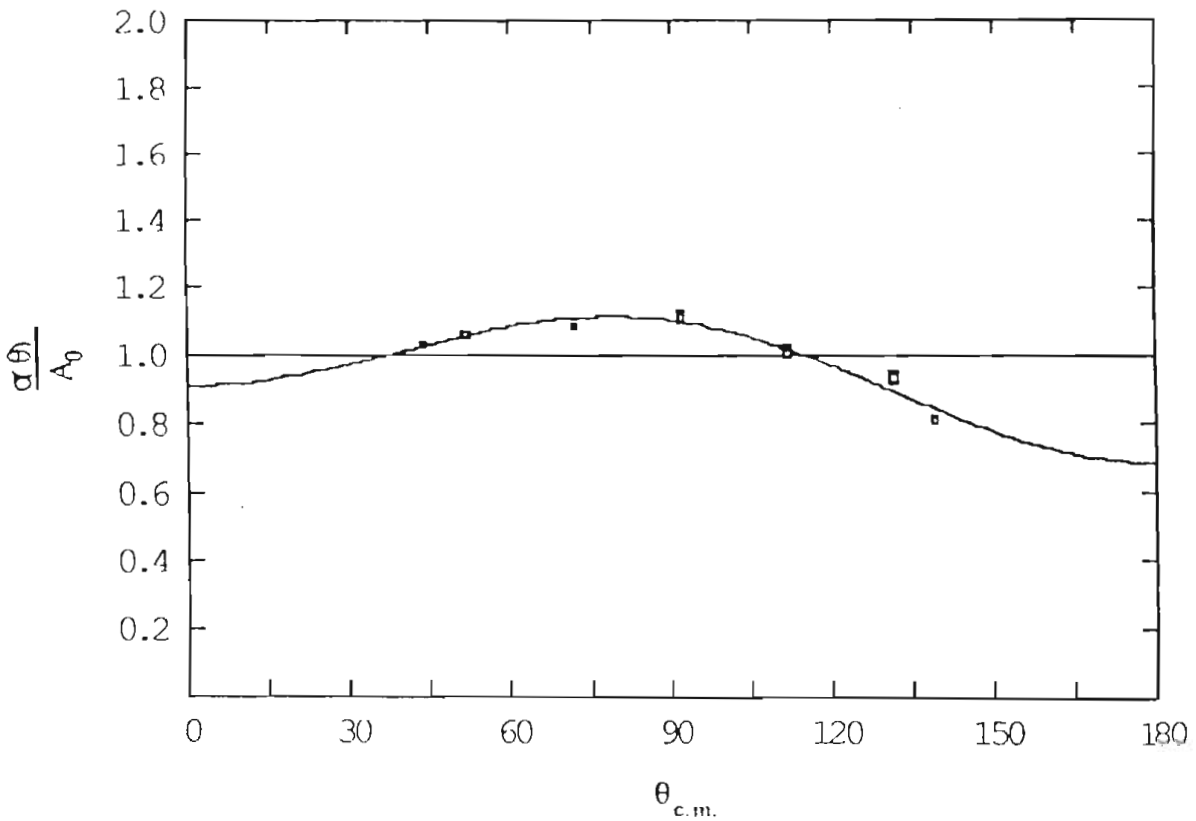
2.0
1.8
1.6
1.4
1.2
1.0
0.8
0.6
0.4
0.2
$\frac{\sigma(\theta)}{A_0}$
0
30
60
90
120
150
180
$\theta_{c.m.}$

Figure 4-5:Legendre polynomial fit obtained using Equation 4-8 for $^{3}H(d,\gamma)^{5}He$ at 8.6 MeV. The error bars represent statistical uncertainties associated with the data points. The solid line is the fit to the data.

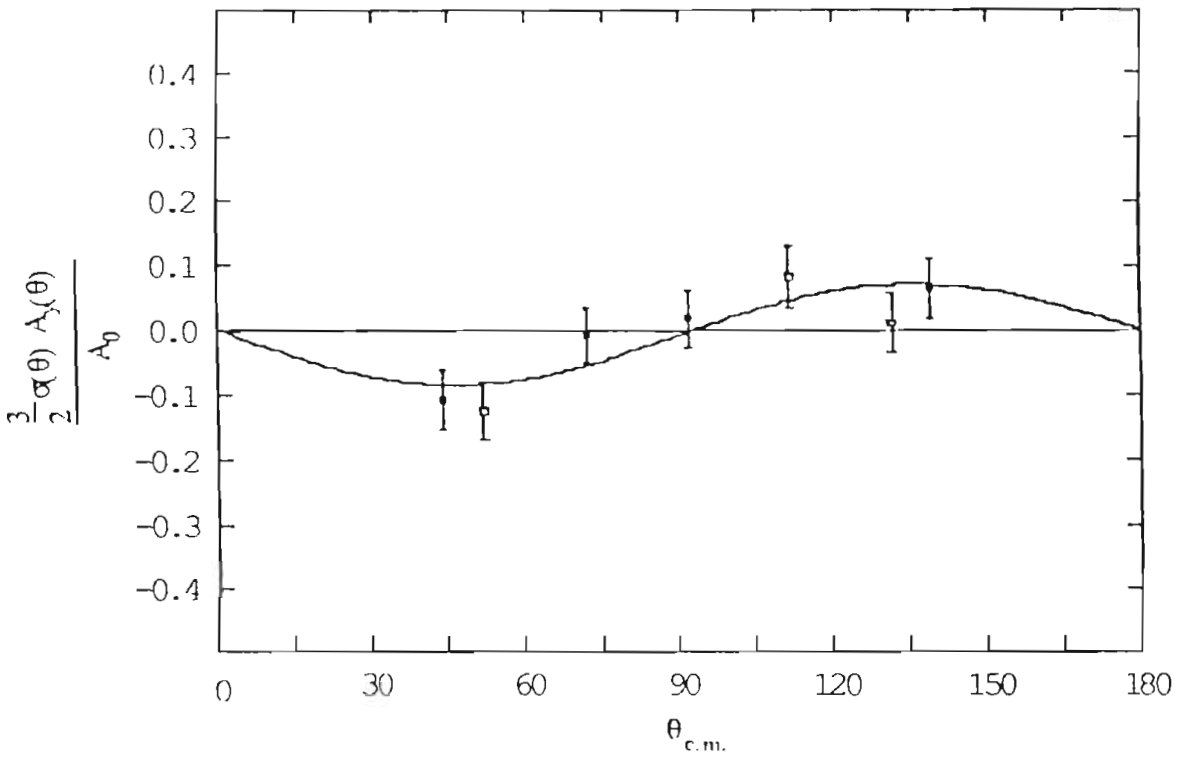
$\frac{3}{2}\frac{\sigma(\theta)\, A_y(\theta)}{A_0}$
0.4
0.3
0.2
0.1
0.0
-0.1
-0.2
-0.3
-0.4
0
30
60
90
120
150
180
$\theta_{c.m.}$

Figure 4-6:Legendre polynomial fit obtained using Equation 4-9 for $^{3}H(d,\gamma)^{5}He$ at 8.6 MeV. The error bars represent statistical uncertainties associated with the data points. The solid line is the fit to the data.

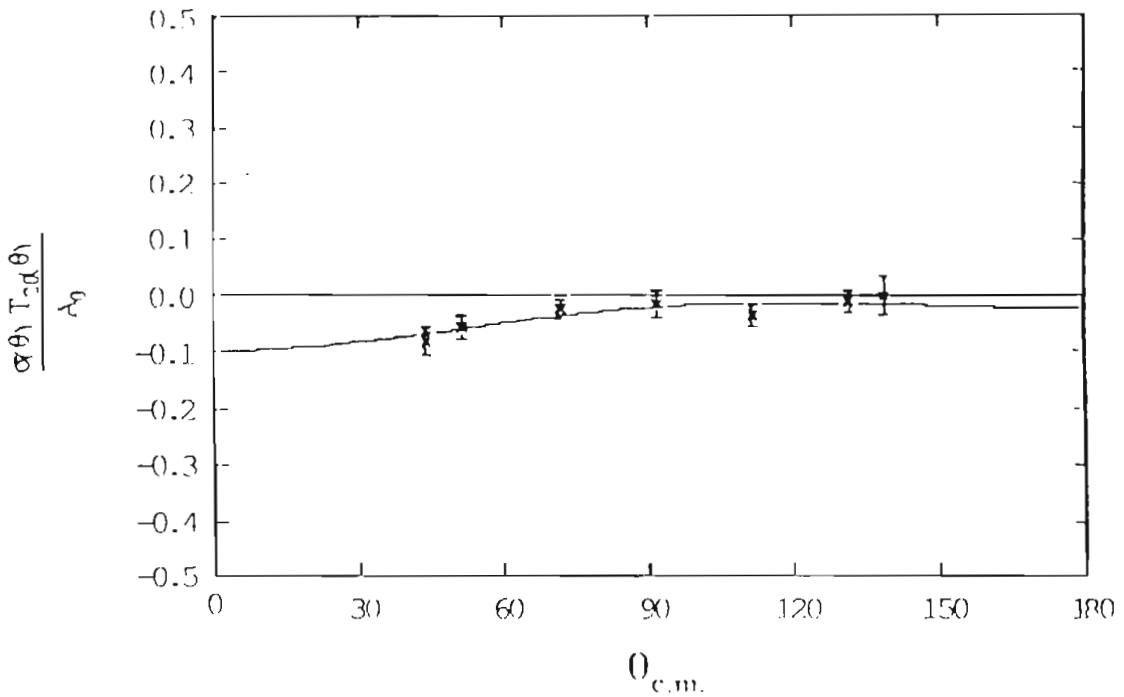
0.5
0.4
0.3
0.2
0.1
0.0
−0.1
−0.2
−0.3
−0.4
−0.5
0
30
60
90
120
150
180
$\theta_{c.m.}$

Table 4-2:Coefficients from Legendre polynomial expansions at 8.6 MeV.

$a_1 = 0.112 \pm 0.014$ $a_2 = -0.206 \pm 0.025$	$b_1 = -0.009 \pm 0.021$ $b_2 = -0.053 \pm 0.014$	$c_0 = -0.0353 \pm .0090$ $c_1 = -0.0371 \pm .0165$ $c_2 = -0.0252 \pm .0306$

4.2 $\sigma(\theta)$, $A_y(\theta)$, and $A_{yy}(\theta)$ at E_d=400keV

In the experiments at low energy, we measured an unnormalized differential cross section $\sigma(\theta)$ at nine angles and $A_y(\theta)$ and $A_{yy}(\theta)$ at seven angles. It should be noted that a deuteron beam with mixed vector and tensor polarizations was used and the tensor analyzing power $A_{yy}(\theta)$ was measured simultaneously with $A_y(\theta)$. With this type of beam, P_y is Q, the percentage polarization of the beam and all three hyperfine states are used to measure $A_y(\theta)$ so that the second part of Equation 4-8 becomes

$$A_y = \frac{1}{p_y} \frac{\sigma_1 - \sigma_3}{\sigma_1 + \sigma_2 + \sigma_3} \qquad 4\text{-}11$$

The cartesian analyzing power $A_{yy}(\theta)$ is related to the spherical tensors by

$$A_{yy}(\theta) = \frac{-1}{\sqrt{2}} T_{20}(\theta) - \sqrt{3} T_{22}(\theta) \qquad 4\text{-}12$$

Measurement of $A_{yy}(\theta)$ allows us to obtain information about the c_k and e_k coefficients of Equation 4-3 by running the source in the mode where $P_z \neq 0$, $P_{zz} \neq 0$, β=90, ϕ=0. With this precession of the beam, $P_y = P_z$, $t_{20} = -P_{zz}/2\sqrt{2}$, t_{21}=0, $t_{22} = -\sqrt{3}P_{zz}/4$. Taking Equation 4-3 for states 1, 2, and 3 (hyperfine states m=1, 0, -1, respectively), and comparing Equation 4-3 with 4-2, we can write from Equation 4-11

$$\frac{\sigma(\theta)A_{yy}(\theta)}{A_0} = \frac{-1}{\sqrt{2}} \sum_{k=0} c_k Q_k P_k(\cos\theta) - \frac{\sqrt{3}}{2} \sum_{k=2} e_k Q_k P_k^2(\cos\theta), \text{ and}$$

$$A_{yy}(\theta) = \frac{1}{p} \frac{\sigma_1 + \sigma_3 - 2\sigma_2}{\sigma_1 + \sigma_2 + \sigma_3} \qquad 4\text{-}13$$

It must be noted here that it was not possible to extract the c_k and e_2 from the data due to the fact that P^2_2 is not orthogonal to the P_k. Since the c_k dominate, the fit given by equation 4-13 was performed without the e_k. However, it was possible to find the e_k by writing the coefficients in terms of amplitudes and phases of the transition matrix elements; this analysis will be presented in Chapter 5.

The differential cross section, $A_y(\theta)$, and $A_{yy}(\theta)$ are shown in Figures 4-7, 4-8, 4-9, respectively and $A_y(\theta)$, and $A_{yy}(\theta)$ are given in Table 4-3. The fits described by the polynomial expressions in equations 4-7, 4-8, and 4-13 are shown in Figures 4-10, 4-11, 4-12, respectively and the coefficients derived are given in Table 4-4.

Figure 4-7:Unnormalized yield $\sigma(\theta)/A_0$ at 400 keV. The error bars represent statistical uncertainties associated with the data points.

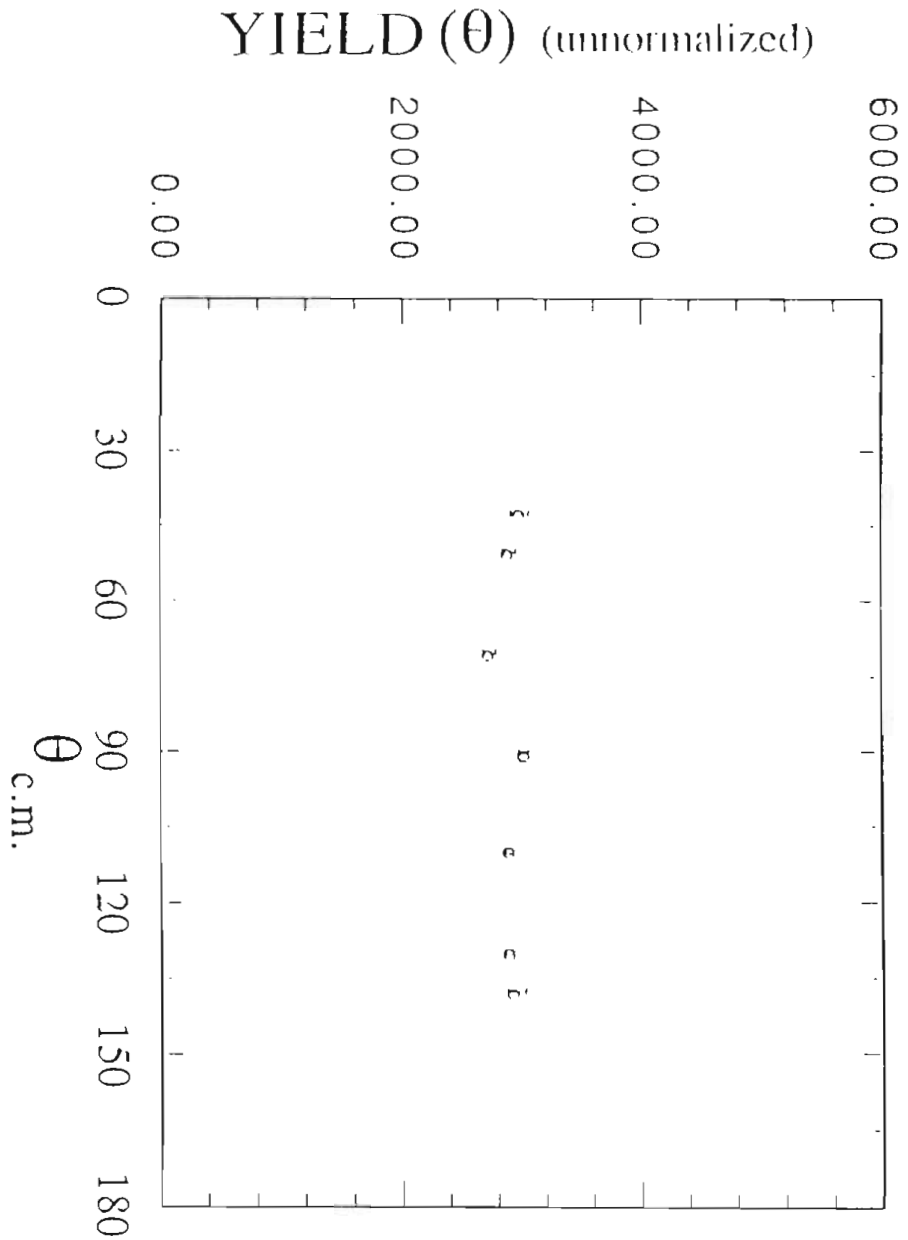
YIELD (θ) (unnormalized)
0.00
2000.00
4000.00
6000.00
0
30
60
90
120
150
180
θ c.m.

Figure 4-8:Vector anayzing power $A_y(\theta)$ at 400 keV. The error bars represent statistical uncertainties associated with the data points.

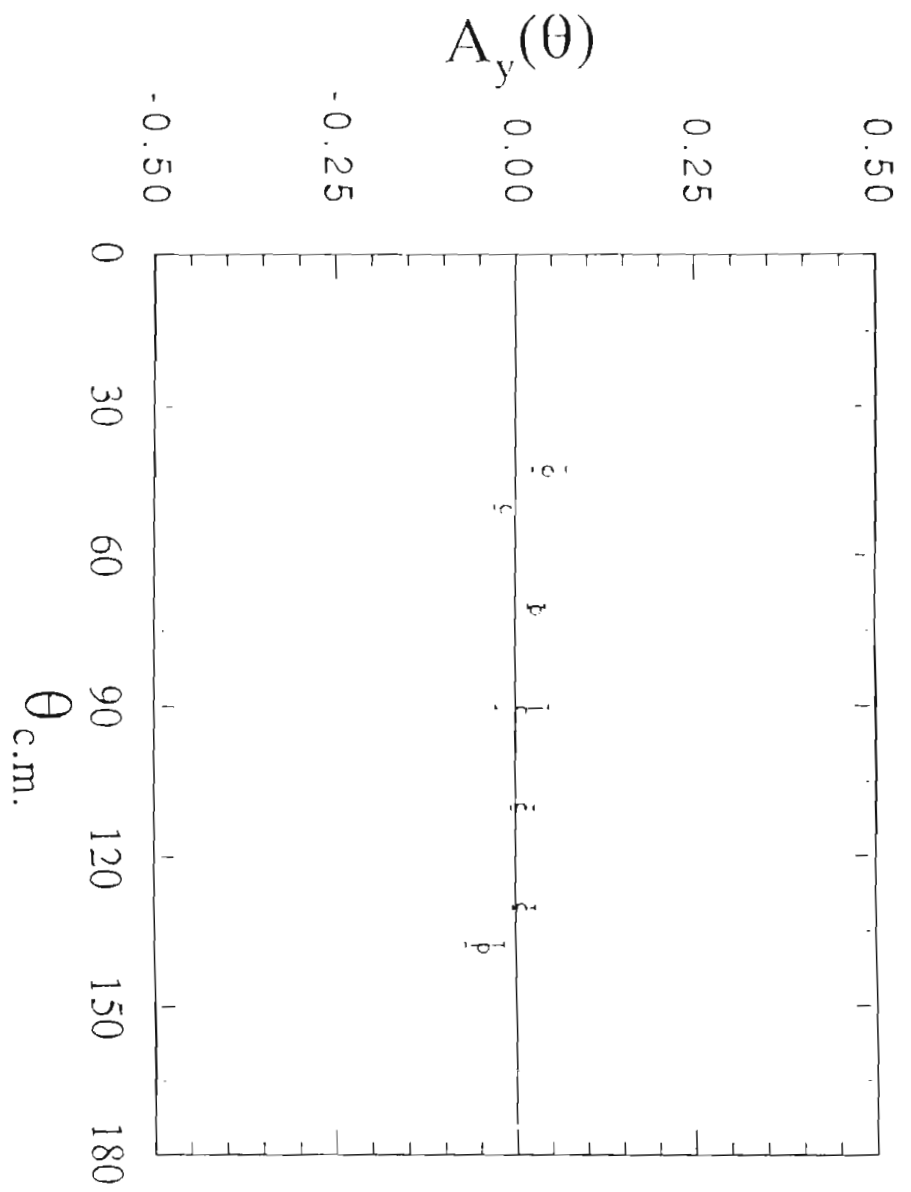
$A_y(\theta)$
0.50
0.25
0.00
-0.25
-0.50
0
30
60
90
120
150
180
$\theta_{c.m.}$

Figure 4-9:Tensor analyzing power $A_{yy}(\theta)$ at 400 keV. The error bars represent statistical uncertainties associated with the data points.

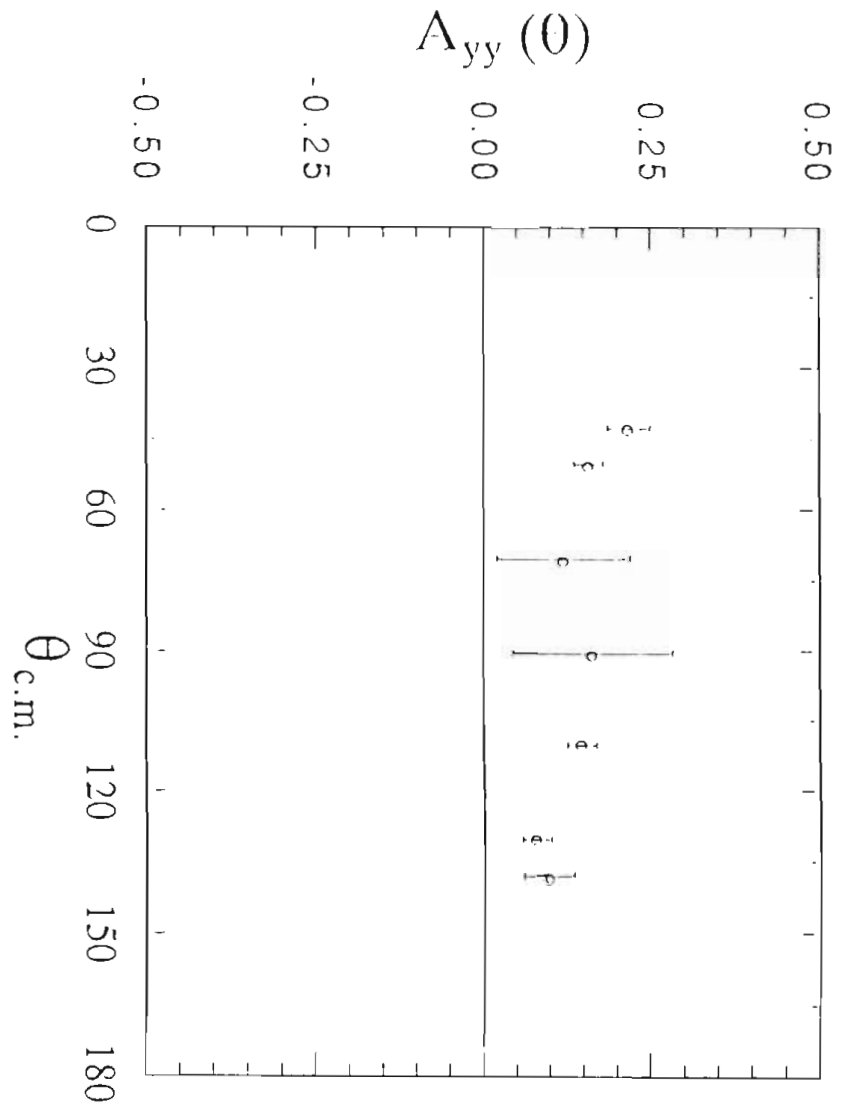
A_{yy} (0)
0.50
0.25
0.00
-0.25
-0.50
0
30
60
90
120
150
180
$\theta_{c.m.}$

TABLE 4-3

$A_y(\theta)$ and $A_{yy}(\theta)$ at 400 keV

θ_{cm}	$A_y(\theta)$	Error $A_y(\theta)$	$A_{yy}(\theta)$	Error $A_{yy}(\theta)$
42.821	0.047	0.024	0.218	0.032
50.364	-0.014	0.016	0.158	0.022
70.446	0.029	0.012	0.120	0.100
90.474	0.0095	0.037	0.164	0.120
110.445	0.0095	0.016	0.148	0.022
130.362	0.011	0.016	0.079	0.022
137.819	-0.044	0.027	0.099	0.037

Figure 4-10: Legendre polynomial fit obtained using Equation 4-7 for $^{3}H(d,\gamma)^{5}He$ at 400 keV. The error bars represent statistical uncertainties associated with the data points. The solid line is the fit to the data.

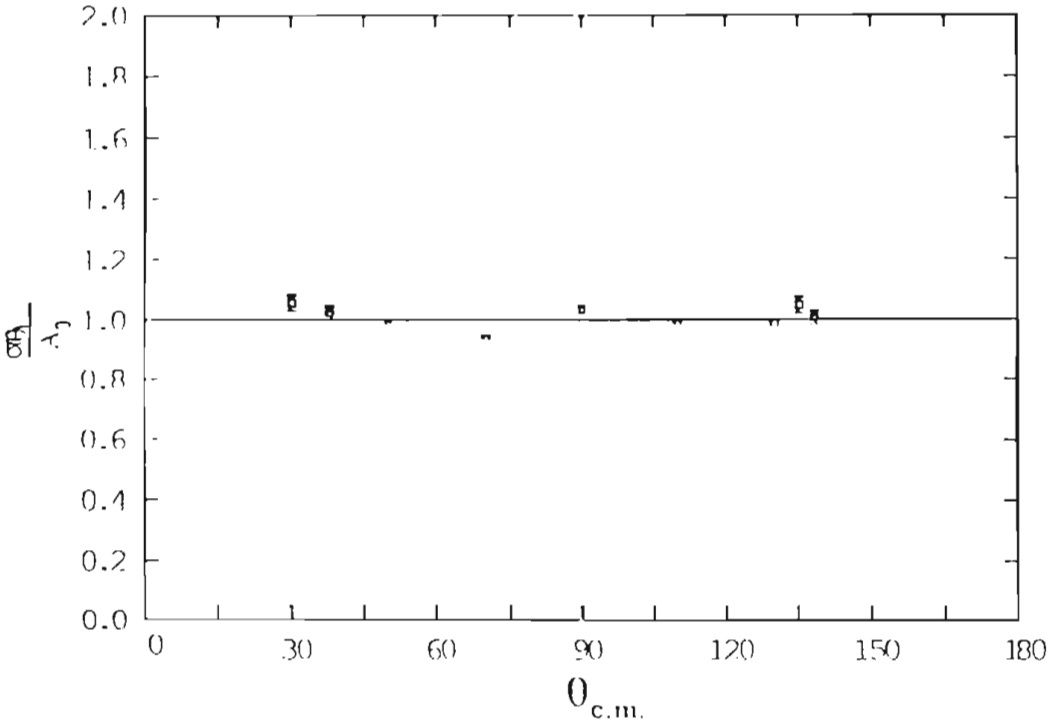
2.0
1.8
1.6
1.4
1.2
1.0
0.8
0.6
0.4
0.2
0.0
0
30
60
90
120
150
180
$\theta_{c.m.}$

Figure 4-11: Legendre polynomial fit obtained using Equation 4-8 for $^{3}H(d,\gamma)^{5}He$ at 400 keV. The error bars represent statistical uncertainties associated with the data points. The solid line is the fit to the data.

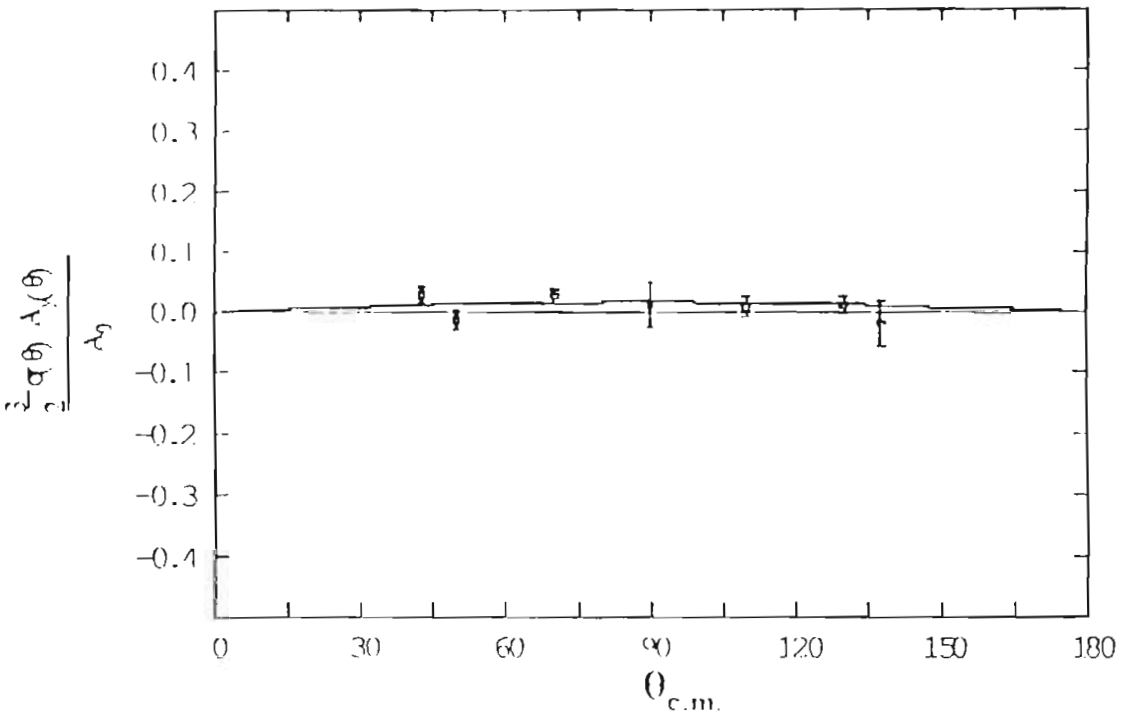
0.4
0.3
0.2
0.1
0.0
−0.1
−0.2
−0.3
−0.4
0
30
60
90
120
150
180
θc.m.

Figure 4-12: Legendre polynomial fit obtained using Equation 4-13 for $^{3}H(d,\gamma)^{5}He$ at 400 keV. The error bars represent statistical uncertainties associated with the data points. The solid line is the fit to the data.

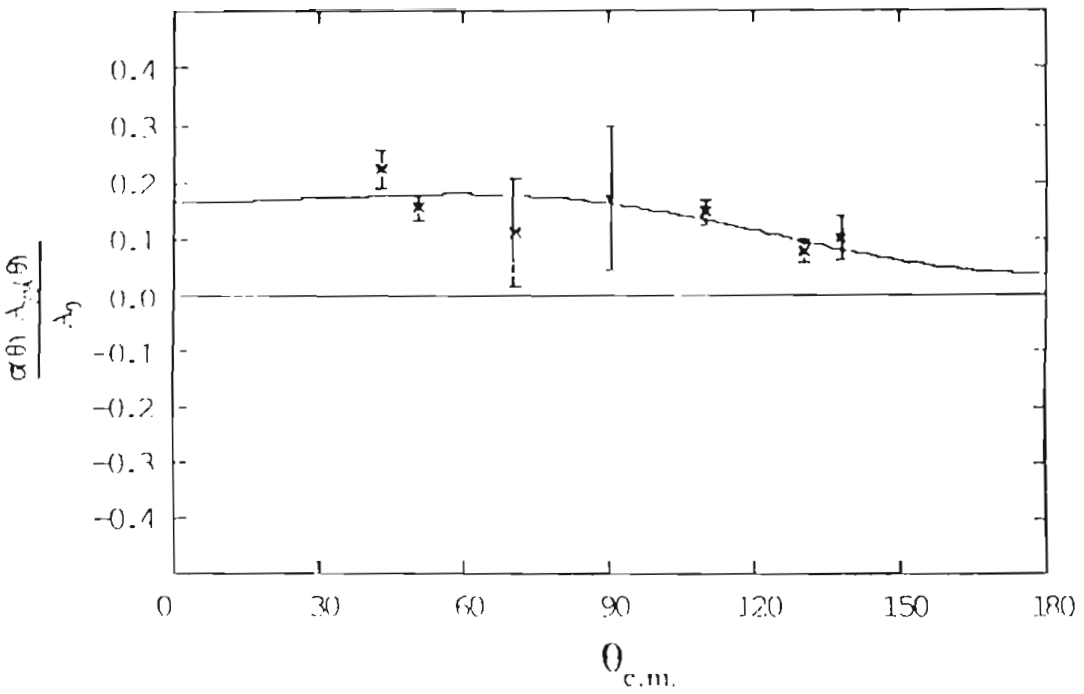
0.4
0.3
0.2
0.1
0.0
-0.1
-0.2
-0.3
-0.4
0
30
60
90
120
150
180
$\theta_{c.m.}$

TABLE 4-4

Coefficients from Legendre polynomial expansions at 400 keV

a1= .002 ± .011
a2= .018 ± .017

b1= -.024 ± .012
b2= -.005 ± .008

c0= -.203 ± .016
c1= -.091 ± .028
c2= .058 ± .070

Chapter 5

TRANSITION MATRIX ELEMENT ANALYSIS OF DATA AT E_d = 400 keV

In chapter 4, the data for cross-section and analyzing powers were fit to Legendre and associated Legendre coefficients. Further analysis of the data is possible by performing a transition matrix element analysis. In this analysis, all of the differential cross section, $A_y(\theta)$, and $A_{yy}(\theta)$ data were simultaneously fit in terms of the amplitudes and phases of the appropriate transition matrix elements. Some simplifying assumptions consistent with angular momentum conservation were made in order to reduce the number of degrees of freedom in the fit due to the large number of amplitudes and phases which could be present.

This simplification was to collapse the j-index of the amplitudes, and search on the percentages of the resulting amplitudes defined by their channel spin $\vec{S}$ and orbital angular momentum $\vec{l}$. This simplification is supported by the findings in elastic scattering phase shift analyses and capture reactions in other light nuclei at low energies which indicate there is little or no $\vec{j}$ dependence in the the transition matrix elements of like $\vec{S}$ and $\vec{l}$ [Jenny, 1980, Skopik, 1979]. If the angular momenta of the $^3H(d,\gamma)^5He$ reaction are written as $\vec{a}(\vec{X},\vec{L})\vec{c}$ where $\vec{a}$ is the spin of the target, $\vec{X}$ is the spin of the projectile, $\vec{L}$ is the multipolarity of the emitted γ-ray, $\vec{c}$ is the spin of the residual nucleus, and $\vec{l}$ is the orbital angular momentum of the deuteron, then

$$\vec{x} + \vec{s} = \vec{S}$$

5-1 $$\vec{l} + \vec{S} = \vec{J}$$

$$\vec{L} + \vec{c} = \vec{J} \quad .$$

From the above, the incident deuteron must have $\vec{l}$=0, 1, 2, 3, or 4. In an E1 transition, conservation of parity allows only $\vec{l}$= 0, 2, or 4 for the incident deuteron. Likewise, in an M1 transition only $\vec{l}$=1 or 3 is allowed. The LS coupling configurations in terms of the above intermediate states and Equations 5-1 are shown for the E1 and M1 transitions in Figure 5-1. For this transition matrix analysis, $\vec{l}$>1 are not included because of the low energy nature of the experiment. The penetrability was calculated for the d-^{3}H system and was found to be 0.2479 for $\vec{l}$=0, 3.097x10^{-2} for $\vec{l}$=1, 6.728x10-4 for $\vec{l}$=2, and 5.288x10^{-6} for $\vec{l}$=3. This rapid decrease in the penetrability by 3 orders of magnitude by $\vec{l}$=2 indicates that it should be justifiable to not include l>1 in the calculation. The notation used for the entrance channel is $^{2S+1}l_J$ (where l=0,1,2 are given by S, P, D respectively.) The different values of J are combined to form ^{2}S (E1), ^{4}S (E1), ^{4}P (M1), ^{2}P (M1) entrance channels so that this analysis could reveal the presence of any M1 radiation and also the predominance of the S=3/2 entrance channel. (This predominance is expected because of the presence of the 3/2$^+$ "fusion" resonance at E_d=107 keV, which is presumably populated with $\vec{l}$=0 and $\vec{S}$=3/2 incoming waves.) The $^{2S+1}l_J$ symbols denote the amplitude of the reduced transition matrix element (T-matrix)

5-2 $$T=\langle pL(C)J\pi||T||l(s_d s_t)SJ\pi\rangle$$

Figure 5-1:LS coupling configurations in terms of the intermediate states given in the text and Equation 5-1 for both E1 and M1 transitions.

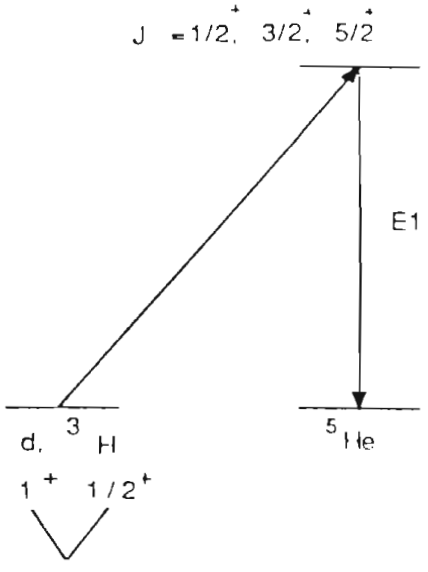

S = 1/2	l = 0	J = 1/2
S = 1/2	l = 2	J = 3/2
S = 1/2	l = 2	J = 5/2
S = 3/2	l = 0	J = 3/2
S = 3/2	l = 2	J = 1/2
S = 3/2	l = 2	J = 3/2
S = 3/2	l = 2	J = 5/2
S = 3/2	l = 4	J = 5/2

l =1, j =3/2-

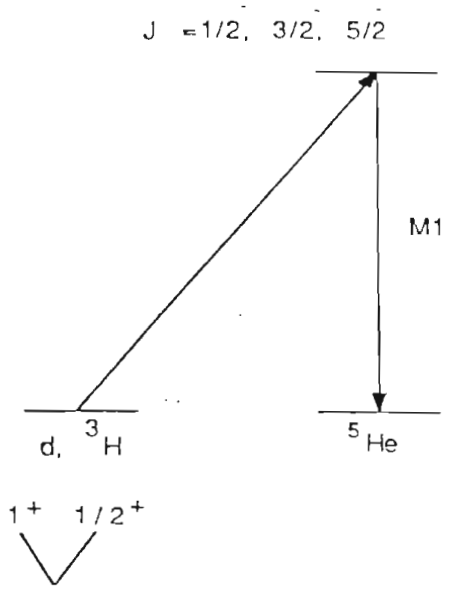

S = 1/2	l = 1	J = 1/2
S = 1/2	l = 1	J = 3/2
S = 1/2	l = 3	J = 5/2
S = 3/2	l = 1	J = 1/2
S = 3/2	l = 1	J = 3/2
S = 3/2	l = 1	J = 5/2
S = 3/2	l = 3	J = 3/2
S = 3/2	l =3	J = 5/2

l =1, j =3/2-

where **C** is the spin of the ground state of ^{5}He, π is the parity of the intermediate state, s_d is the spin of the deuteron, s_t is the spin of the triton, and the operator T is the interaction multipole operator. Since this matrix element is a complex number, each amplitude has a corresponding phase. The coefficients of the Legendre and associated Legendre expansions of the cross section and analyzing powers (Equations 4-7, 4-8, 4-13) can be expressed in terms of the T-matrix amplitudes and phases [Seyler and Weller, 1979]. These equations are listed in the appendix. The resulting expressions for $\sigma(\theta)/A_0$, $A_y(\theta)$, and $A_{yy}(\theta)$ were then used to fit the measured values in terms of ^{2}S, ^{4}S, ^{2}P, and ^{4}P amplitudes and their relative phases by the non-linear regression routine NREG. The results of this fit are shown in Table 5-1 and Figure 5-2. The ^{4}S (E1) amplitude predominates with 95% of the strength, with 2.5% in the ^{2}S(E1) and 2.5% M1 strength. The Legendre polynomial coefficients resulting from this fit are compared with those presented in Chapter 4 in Table 5-2. A list of the Legendre coefficients in terms of these j-independent transition matrix elements is given in the Appendix. A fit with similar χ^2 but different phases for the ^{2}P and ^{4}P , -72.68 and 51.85 degrees respectively, allows 7.66% M1 radiation and 2.93% ^{2}S (E1) radiation. This is in contrast to the previous analysis of the ^{3}H(d,n)^{4}He cross section data [Jarmie, 1984] which indicates that essentially no S=1/2 background was present in the energy region below 250 keV in the neutron channel. The present results indicate the power of the tensor polarized deuteron capture technique as a tool for sensing small portions of the ground state wavefunction.

Table 5-1: Amplitudes and phases found by transition matrix analysis of $\sigma(\theta)/A_0$, $A_y(\theta)$, and $A_{yy}(\theta)$ for $^3H(d,\gamma)^5He$ at 400 keV.

TABLE 5-1

MATRIX ELEMENT	RELATIVE INTENSITY	PHASE ANGLE (DEG.)
^2S	0.026 ± .005	174.34 ± .49
^4S	0.949 ± .067	0.00 ± 0.0
^2P	0.005 ± .003	4.15 ± .22
^4P	0.020 ± .005	-0.14 ± .86

Figure 5-2 (three pages): Fits to $\sigma(\theta)/A_0$, $A_y(\theta)$, and $A_{yy}(\theta)$ by transition matrix analysis at 400 keV. The solid line represents the fit. All error bars are purely statistical.

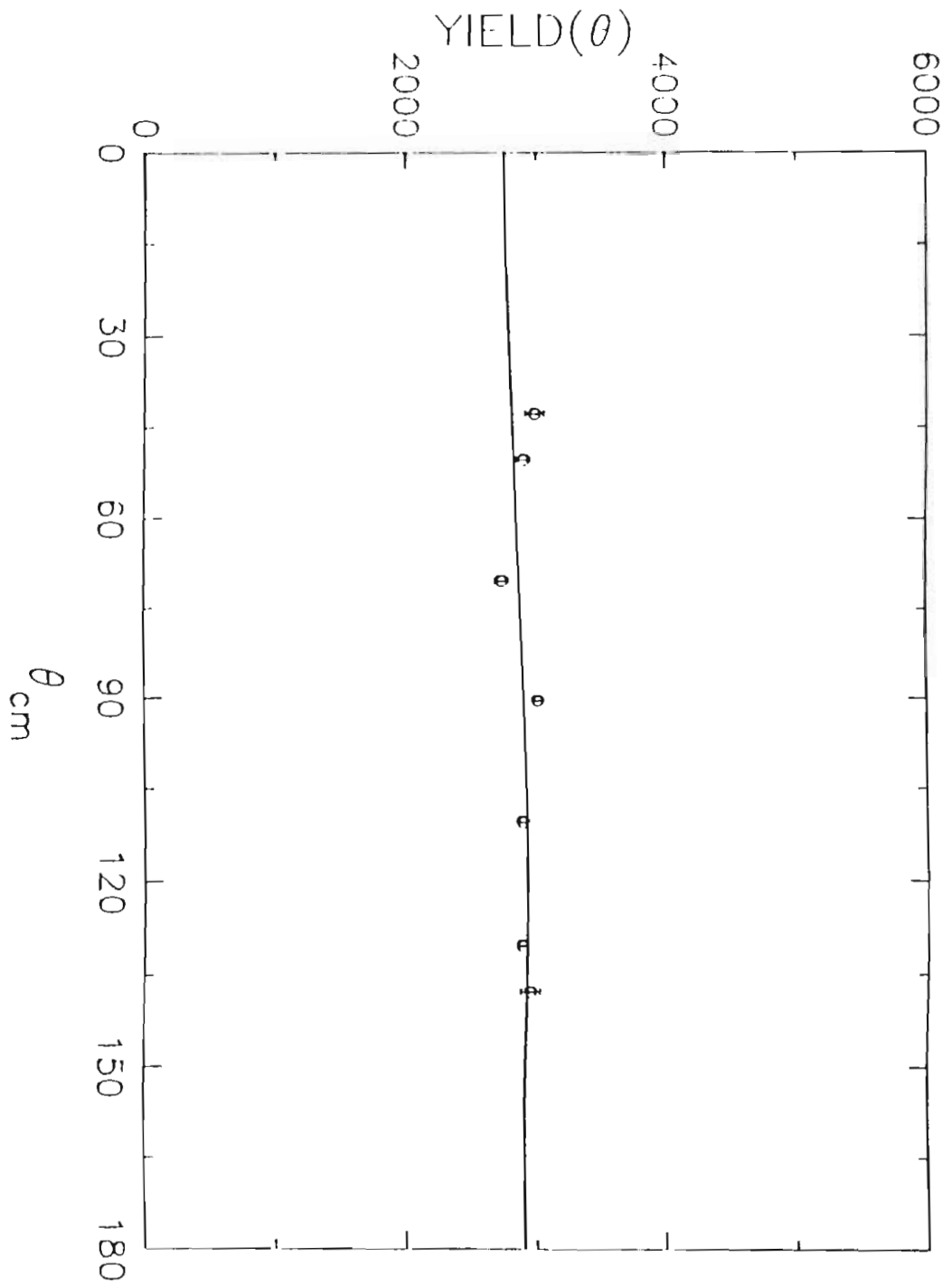
YIELD(θ)
0
2000
4000
6000
0
30
60
90
120
150
180
θcm

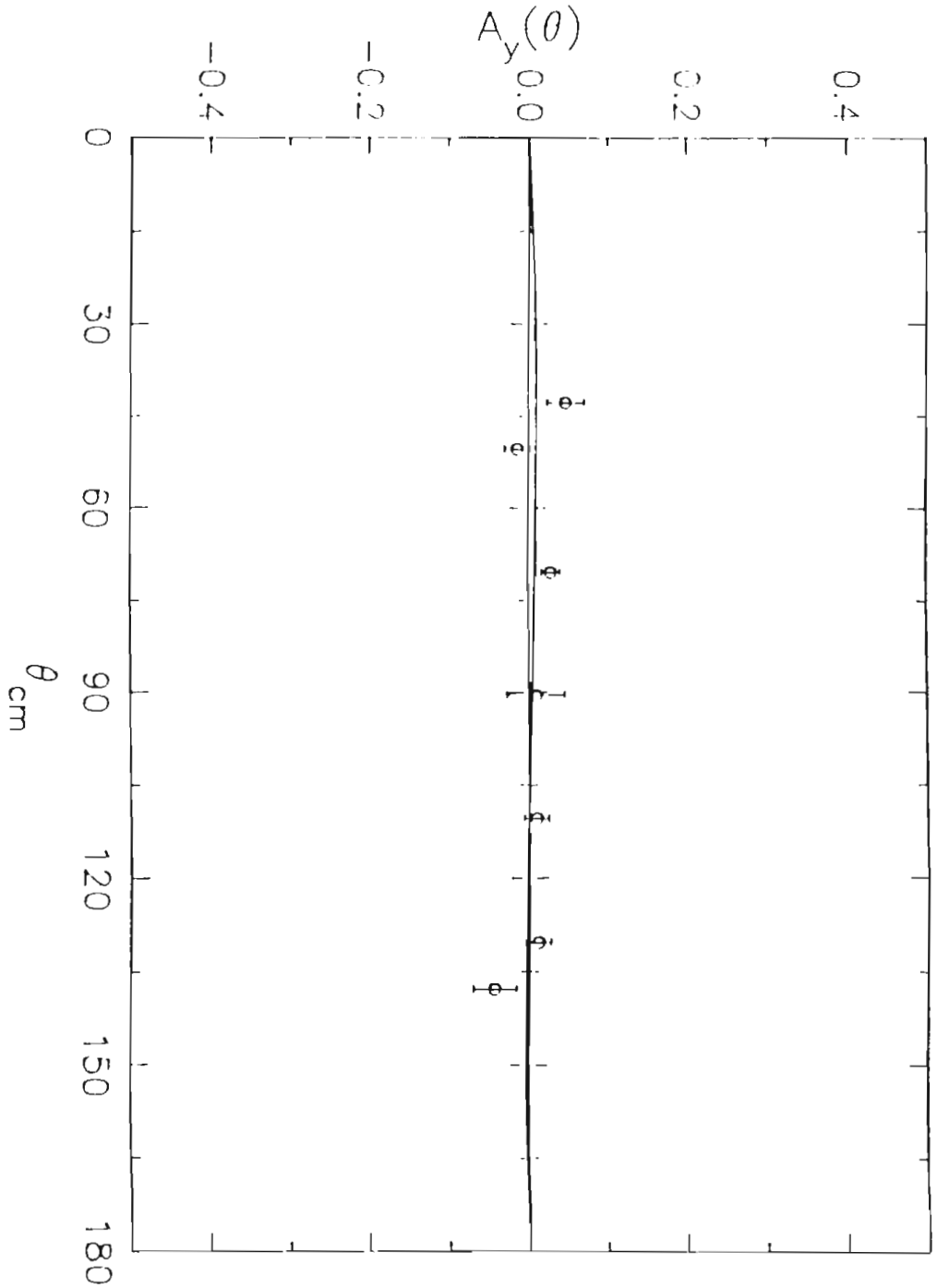
$A_y(\theta)$
−0.4
−0.2
0.0
0.2
0.4
0
30
60
90
120
150
180
θ_{cm}

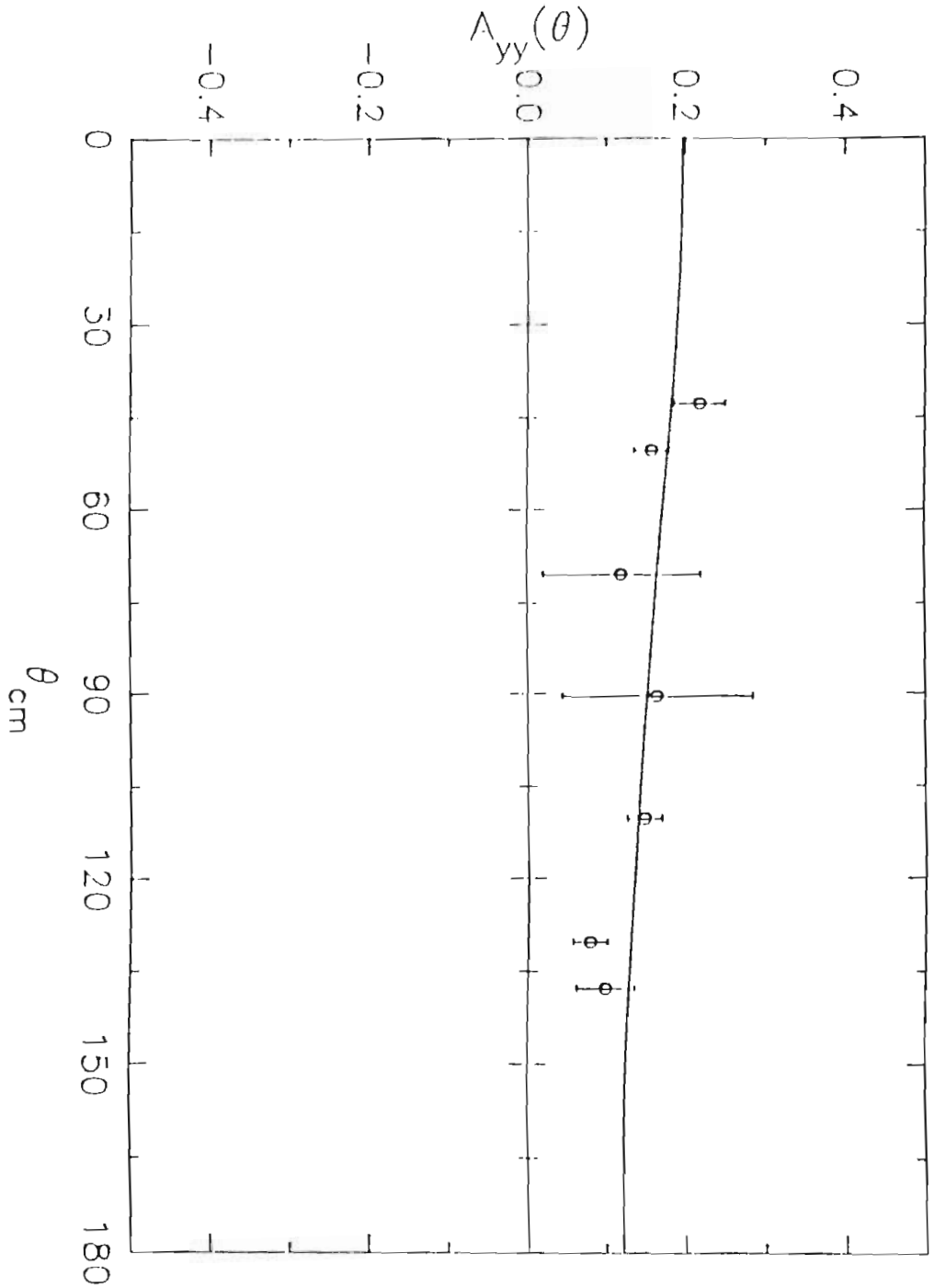
$A_{yy}(\theta)$
−0.4
−0.2
0.0
0.2
0.4
0
30
60
90
120
150
180
θ_{cm}

Table 5-2: Comparison of Legendre polynomials coefficients obtained in Chapter 4 and those obtained by the transition matrix element analysis.

TABLE 5-2

FROM LEGENDRE POLYNOMIAL FITS	TRANSITION MATRIX ELEMENTS ANALYSIS
a1= .002 ± .011	a1= -.026 ± .008
a2= .018 ± .017	a2= -.018 ± .005
b1= -.024 ± .012	b1= .007 ± .004
b2= -.005 ± .008	b2= .007 ± .002
c0= -.203 ± .016	c0= .002 ± .001
c1= -.091 ± .028	c1= -.046 ± .013
c2= .058 ± .070	c2= -.219 ± .018
	e2= -.089 ±.007

Chapter 6

DIRECT CAPTURE CALCULATIONS AT 8.6 MeV

A direct-capture calculation was carried out for the $^{3}H(d,\gamma)^{5}He$ reaction at 8.6 MeV using a d-^{3}H cluster model. This model is expected to be valid at this energy since no resonance-like behavior has been reported here, in contrast to the situation at E_d=400keV. In this manner we may calculate the relative strengths of the T-matrix elements and thus the reaction observables. The a_k, b_k, c_k and e_k coefficients were generated also to compare with the experimental results.

Capture reactions are transitions from an initial continuum scattering state to the ground state of the compound nucleus by interaction with the electromagnetic field. The theory of direct capture reactions has been described in detail by [Brown, 1964,; Rolfs, 1973; Dietrich, 1977] and only a brief discussion will be presented here.

In this theory, the initial continuum state may be described by a distorted wave with the interaction Hamiltonian represented by the electromagnetic operator, and the final state described as a standing wave of specific orbital angular momentum. The radial part of the transition matrix elements is given [Weller, 1980] by

$$R=\langle u_b | r^L | X^+ \rangle \quad . \tag{6-1}$$

Where r^L is the radial part of the electromagnetic operator of multipolarity L in the long wavelength approximation. For E1 transitions, this is just r. X^+ is

the continuum state distorted by the optical potential, and u_b is the radial part of the bound state. Calculation of the radial matrix elements was performed by the code RADCAP.

The initial-state wave functions are obtained using an optical model potential with radial form

6-2 $$V(r) = V_c(r) + V_n(r) + W_n(r) + V_{so}(r)\ \vec{l}\cdot\vec{S}$$

where $V_c(r)$ is the coulomb potential between the deuteron and the triton, which were treated as a uniformly charged spheres, $V_n(r)$ is the real central potential which has a Woods-Saxon shape, $W_n(r)$ is the imaginary central potential which has a surface-derivative Woods-Saxon form, and $V_{so}(r)$ is the spin-orbit potential, which, because of calculational considerations, was added into the central potential for different values of $\vec{l}\cdot\vec{S}$ instead of the usual method of treating it as a surface derivative term. This procedure has previously been used in describing the $^4He(d,\gamma)^6Li$ reaction [McIntyre and Haeberli]. The Woods-Saxon form factor is given by

6-3 $$f(r,r_0,a_0)=[1+\exp[(r-r_0)/a_0]]^{-1}$$

Because of the lack of optical model parameters for this reaction at this energy, the parameters used for the continuum state were the same as for the bound state, with a spin-orbit potential taken from [Perey and Perey, 1976]. The bound state wave function used in RADCAP was calculated by adjusting the well depth of the Woods-Saxon in the real part of the optical model potential to obtain the correct binding energy for ^5He. In the present case, the ground state is actually unbound with respect to neutron emission. However, it is bound in the $d+^3H$

channel and was treated as a bound state (no width) in the present calculation.

The transition matrix elements in the jj coupling scheme may be obtained from the radial matrix elements R given in Equation 6-1 by [Weller, 1980]

$$T^{L}_{l_j,l_a j_a} = i^{l_a - l - L} C(j\ L\ j_a, 1/2, 0, 1/2) \sqrt{C^2 S_{lj}}\, \frac{j}{j_a} R^{L}_{lj,l_a j_a} \qquad 6\text{-}4$$

where l_a and j_a are the orbital and total angular momenta of the incident particle, land j are the orbital and total angular momenta of the final bound state with spectroscopic factor C^2S_{lj} (C being the isospin Clebsh-Gordon coefficient), and L is the multipolarity of the γ-ray. $\mathbf{j}$ is given by

$$\mathbf{j} = (2j+1)^{1/2} \qquad 6\text{-}5$$

The resulting transition matrix element is a complex number represented by a real amplitude and a phase angle. These matrix elements were then transformed from the jj coupling scheme to the LS coupling scheme using the prescription of [Seyler and Weller, 1979].

This calculation included only E1 radiation. Referring to Fig. 5-1, which shows the allowed angular momentum combinations allowed for this reaction, we can see that there are two channel-spins available in this reaction: $\vec{S}$=1/2 and $\vec{S}$=3/2. The transition matrix elements were arranged into $\vec{S}$=1/2 and $\vec{S}$=3/2 and admixed by

$$\rho |\vec{S}=1/2\rangle + \sqrt{(1-\rho^2)}\, |\vec{S}=3/2\rangle = \psi_{g.s.} \qquad 6\text{-}6$$

The Legendre coefficients a_1, a_2, b_1, b_2, c_0, c_1, c_2, from equation 4-7, 4-8 and 4-9 were then generated from the transition matrix elements [Seyler and Weller, 1979] with ρ varied from 0 to 1.0 to judge what percent admixture of $\vec{S}$=3/2 was necessary for the experimentally derived coefficients. The results of a calculation with no spin-orbit interaction are shown in Figure 6-1. This comparison suggests an admixture of between 35% and 75% $\vec{S}$=3/2 from the b_2, c_0, and c_2 coefficients, whereas for b_1 the experimental value is consistent with zero and the theoretical calculation is zero for all admixtures. The a_1, a_2, and c_1 coefficients do not compare as well to the experimentally derived values. a_1 and c_1 calculations are zero for all admixtures in contrast to the non-zero experimental values, whereas the calculated value for a_2 is approximately twice the magnitude of a_2. Most likely, the reason for these disparities is the lack of non-E1 radiation in the calculation. Optical model parameters used in this calculation are given in Table 6-1.

TABLE 6-1

Parameters Used in the Optical Model for the Bound State

V_n=-93.16 W_n=0 r_o=1.25 a=.65

Parameters Used in the Optical Model for the Continuum State

V_n=-93.16 W_n=0 r_o=1.25 a=.65

Figure 6-1 (two pages): Comparison of Legendre polynomial coefficients obtained in Chapter 4 for $^{3}H(d,\gamma)^{5}He$ at 8.6 MeV and those generated by the direct-capture calculation described in the text. The shaded areas represent the experimentally determined coefficients and their statistical errors. The solid lines represent the calculated values with no spin-orbit interaction.

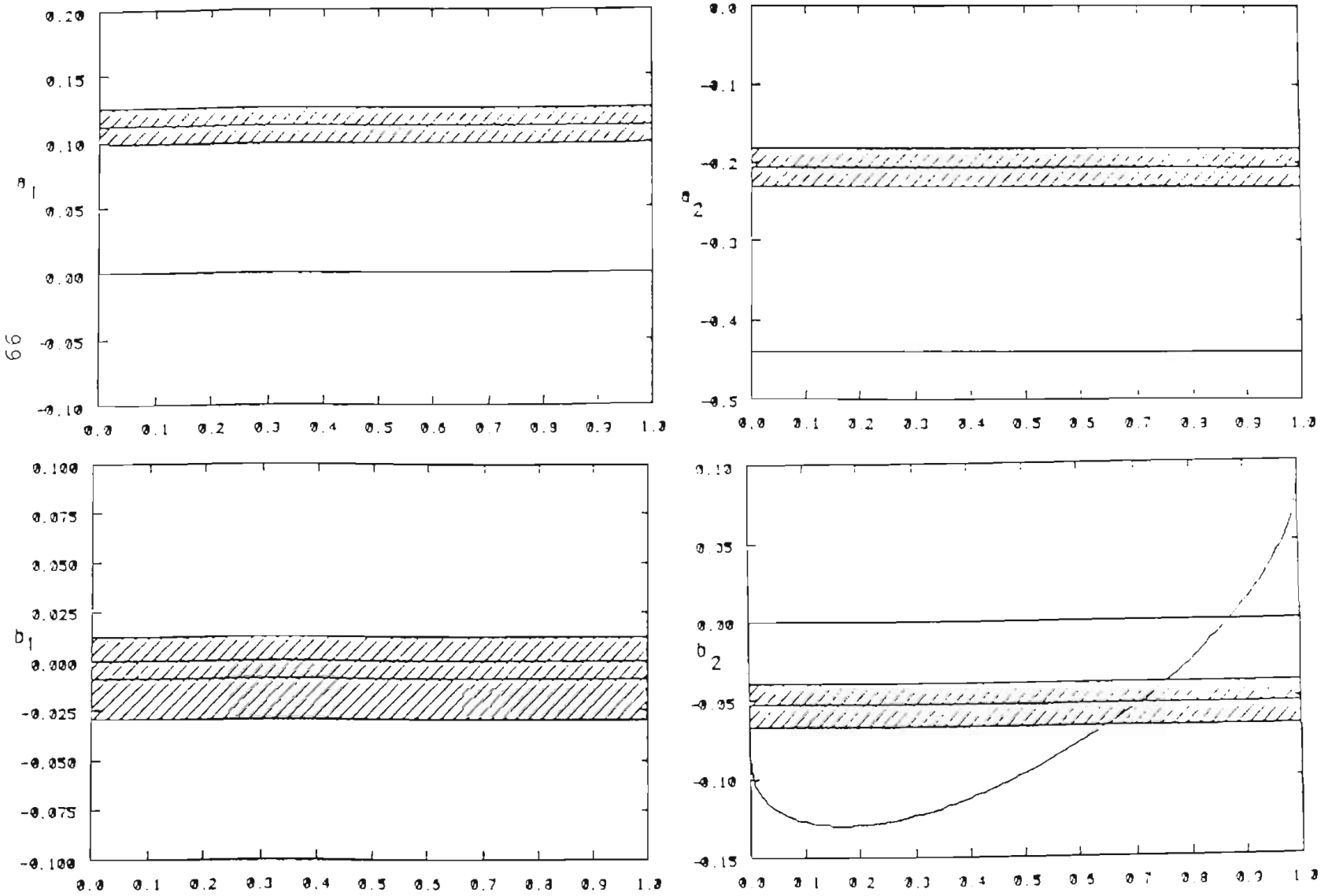
a1
a2
b1
b2
99

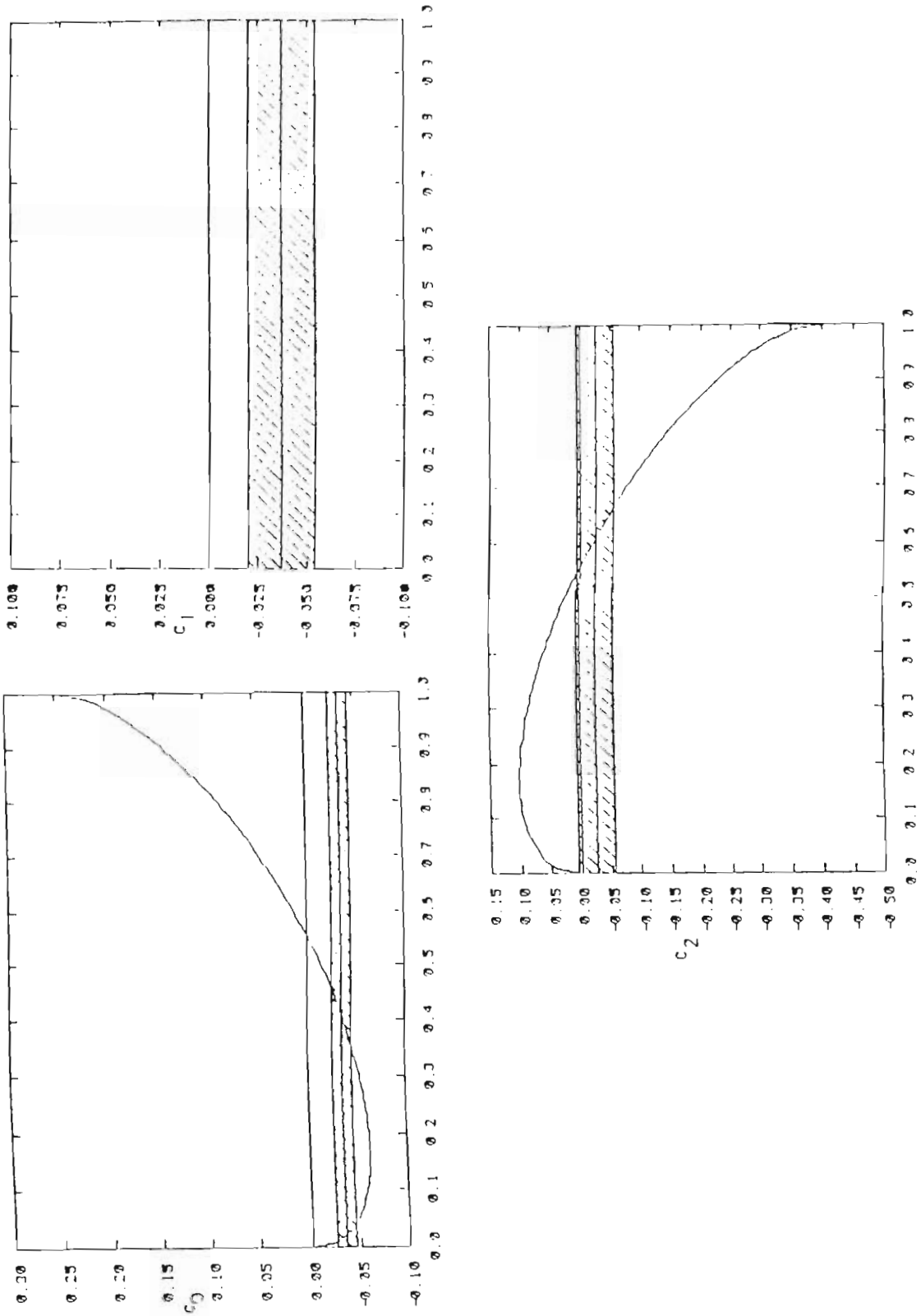
c_0
c_1
c_2

In an effort to better determine the amount of $\vec{S}=3/2$ necessary to get the best agreement with the data, a spin-orbit potential was added to the optical model potential used previously. It was thought that perhaps the vector analyzing power could be more effectively represented by a spin-orbit interaction. The results are shown in Fig 6-2. The calculated values for a_1, and c_1 remained zero, which they must for a pure E1 calculation. The calculated value of a_2 was brought nearer to the experimental value and the amount of $S=3/2$ necessary for agreement with b_2, c_0, and c_2 was raised to a range of 88% to almost 100%, with b_1 still zero in agreement with the experimental value for any admixture. Optical model parameters used in this calculation with a spin-orbit interaction are given in Table 6-2.

TABLE 6-2

Parameters Used in the Optical Model for the Bound State

V_n=-93.16 W_n=0 r_o=1.25 a=.65

Parameters Used in the Optical Model for the Continuum State

V_n=-93.16 W_n=0 r_o=1.25 a=.65 V_{so}=5 MeV.

These data are therefore consistent with a E1 strength which is 88-100% $\vec{S}=3/2$ when a spin-orbit interaction is introduced. The ground state is found to be 88-100% $\vec{S}=3/2$ in this model calculation. This result

is consistent with the result obtained at low energies in Chapter 5 (95% S=3/2 E1).

Figure 6-2 (two pages):Comparison of Legendre polynomial coefficients obtained in Chapter 4 for $^{3}H(d,\gamma)^{5}He$ at 8.6 MeV and those generated by the direct-capture calculation described in the text. The shaded areas represent the experimentally determined coefficients and their statistical errors. The solid lines represent the calculated values with a spin-orbit interaction.

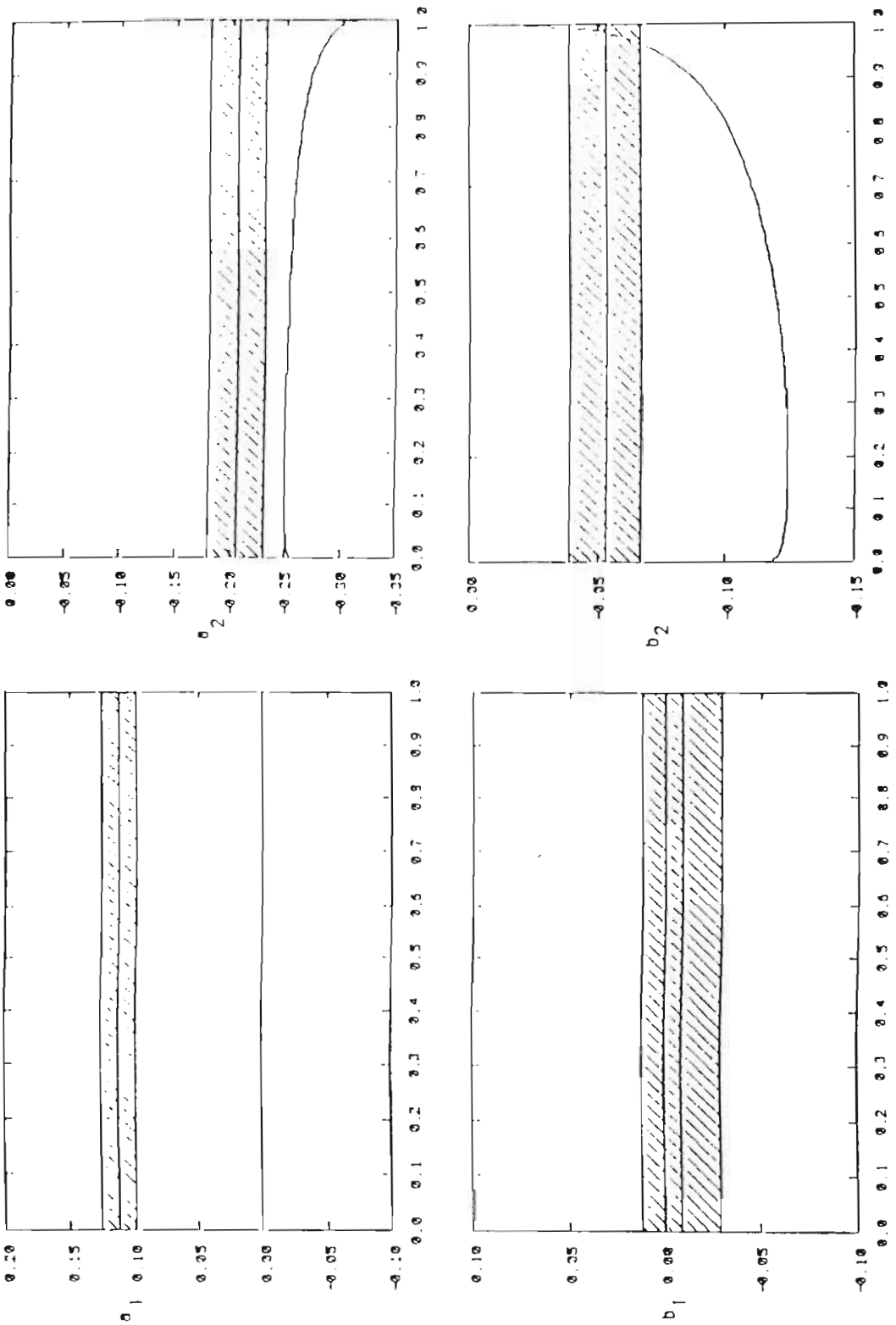
a_2
b_2
a_1
b_1

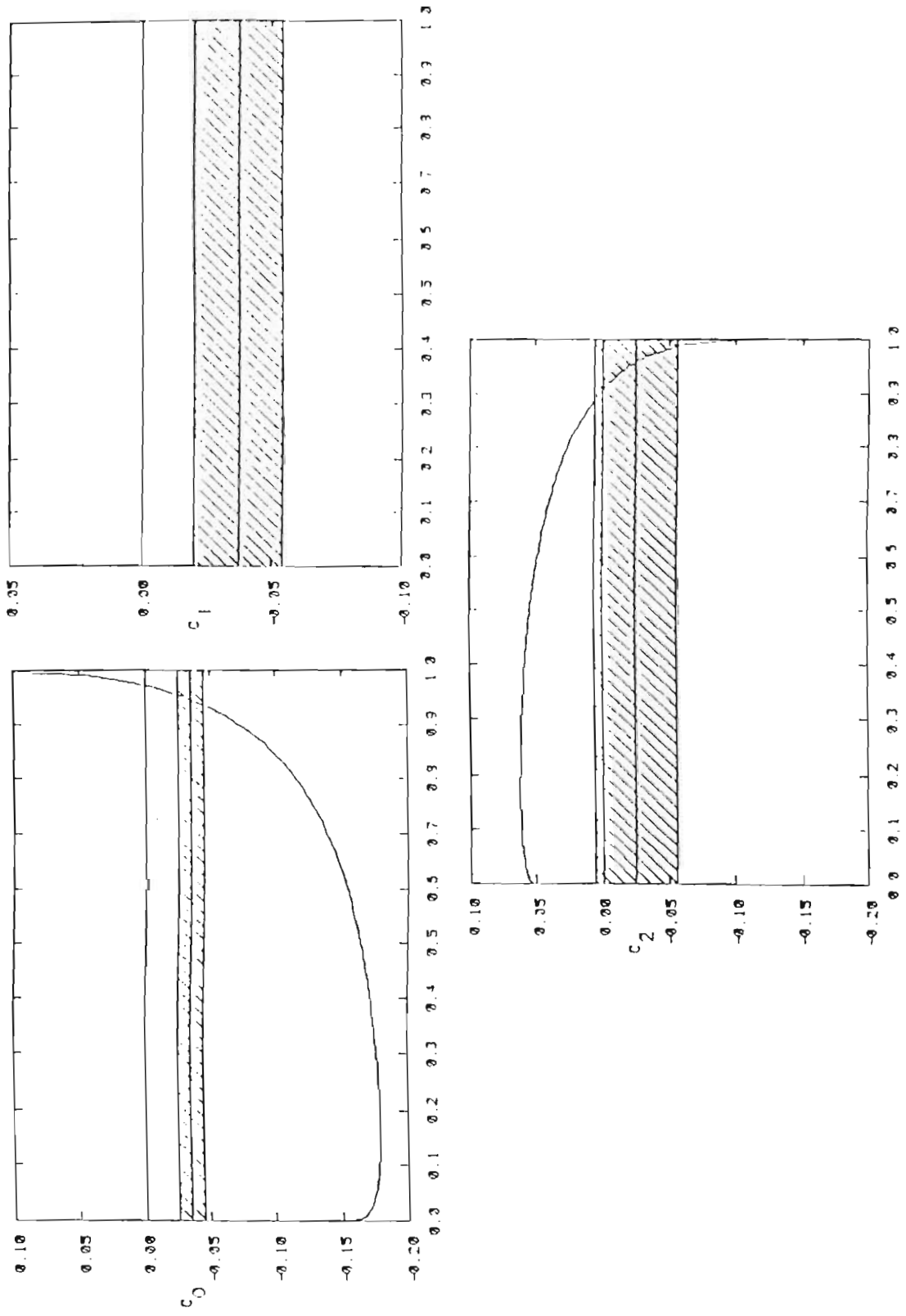
0.35
0.30
-0.05
-0.10
c_1
0.10
0.05
0.00
-0.05
-0.10
-0.15
-0.20
c_0
0.10
0.05
0.00
-0.05
-0.10
-0.15
-0.20
c_2

Chapter 7

Conclusions

Through the measurement of cross section and analyzing powers of the $^{3}H(d,\gamma)^{5}He$ reaction, it has been possible to draw some conclusions about the reaction.

The transition matrix element analysis of the data obtained at E_d = 400 keV indicates that the reaction proceeds primarily by the S=3/2 channel via E1 radiation with 95% strength in the ^{4}S amplitude, with 2.5 % strength in the ^{2}S (E1) amplitude and 2.5% strength in the ^{4}P and ^{2}P (M1) amplitudes. This indicates the usefulness of tensor polarized deuteron capture in determining the presence of small transition amplitudes which contribute to the reaction.

An E1 direct capture d-^{3}H cluster model calculation was performed at 8.6 MeV to calculate the relative strength of the T-matrix elements and thus the reaction observables. It was found that if a spin-orbit interaction was included in calculating the continuum wavefunction, then the data were consistent with a 88-100% S =3/2 component in the ground state of ^{5}He. This result is also consistent with the 95% S =3/2 E1 strength found through a transition matrix element analysis for the data at E_d= 400 keV since this E1 strength is predominantly $\Delta\vec{S}$ strength. Unfortunately, this direct capture calculation cannot be performed at 400 keV because of the presence of resonant behavior in this energy region.

APPENDIX

Legendre polynomial coefficients in terms of the transition matrix amplitudes and phases

$$A_0 = 2|^2S|^2 + 4|^4S|^2 + 6|^2P|^2 + 12|^4P|^2$$

$$a_1 = 8.325\ {}^2S\ {}^2P \cos(T_{2P} - T_{2S})$$

$$a_2 = 2.865\ |^2P|^2 - 12|^2P|^2$$

$$b_1 = -1.162\ {}^2S{}^2P \sin(T_{2P} - T_{2S}) - 4.243\ {}^2S{}^4P \sin(T_{4P} - T_{2S}) + 3.581\ {}^4S\ {}^2P \sin(T_{2P} - T_{4S}) - 13.416\ {}^4S\ {}^4P \sin(T_{4P} - T_{4S})$$

$$b_2 = -0.632\ |^2P|^2 - 2.943\ {}^2P\ {}^4P \sin(T_{4P} - T_{2P}) + 4.6\ |^4P|^2$$

$$c_0 = 1.47\ {}^2P\ {}^4P \cos(T_{4P} - T_{2P})$$

$$c_1 = -3.341\ {}^4S\ {}^2P \cos(T_{2P} - T_{4S})$$

$$c_2 = -0.894\ {}^2S\ {}^4S \cos(T_{4S} - T_{2S}) - 1.131\ |^4S|^2 - 1.47\ {}^2P\ {}^4P \cos(T_{4P} - T_{2P})$$

$$e_2 = -0.365\ {}^2S\ {}^4S \cos(T_{4S} - T_{2S}) - 0.462\ |^4S|^2$$

Note: In the transition matrix element calculation, T_{4S} is arbitrarily set equal to zero. The notation $T_{(2s+1)(l)}$ represents the phase of the transition matrix element whose amplitude is denoted by ${}^{2S+1}L$. L=0 (S- wave) amplitudes correspond to E1 transitions, while L=1 (P- wave) amplitudes are M1 transitions.

LIST OF REFERENCES

H.H. Barschall and W. Haeberli, eds., *Polarization Phenomena in Nuclear Reactions*, Proc. of the Third Inter. Symp., Madison, WI, 1970

P.A. Batay-Csorba and C.A. Barnes Bull. Am. Phys. Soc. 20 829 (1975)

V.M. Bezotsnyi, V.A. Zhmaylo, L.M. Surov, and M.S. Shvetsoy Sov. Jour. Nucl. Phys. 10 127 (1975)

J.E. Brolley, T.M. Putnam, L. Rosen, L. Stewart, Phys. Rev. 117, (1960) 1307

G.E. Brown, Nucl. Phys. 57 (1964) 339

W. Buss, H. Waffler and B. Ziegler Phys. Lett. 4 (1963) 198

F.E. Cecil, D.M. Cole and F.J. Wilkinson III, Nuc. Inst. and Meth. B10/11, 411 (1985)

T.B. Clegg, G.A. Bissinger and T.A. Trainor, Nucl. Instr. Meth. 120 (1974) 445

S.E. Darden, "Description of Polarization and Suggestions for Additional Conventions" in Barschall and Haeberli (1970), p. 39

F.S. Dietrich, D.W. Heikkinen, K.S. Snover and K. Ebisawa, Phys. Rev. Lett. 38 (1977) 156

G. Feldman, personal cummunication, 1989

H.A. Grunder, R. Gleyvod, J. Lietz, G. Morgan, H. Rudin, F. Seiler and A. Stricker, Helvetica Physica Acta 44 662 (1971)

N. Jarmie et al., Phys. Rev. C 29, (1984) 2031

B. Jenny et al., Nucl. Phys. A337 (1980) 77

S.E. King, unpublished Ph.D. Dissertation, Duke University, 1983

A. Kosiara and H.B. Willard Phys. Lett. 32B 99 (1970)

J.B. Marion and F.C. Young, Nuclear Reaction Analysis, North Holland, Amsterdam, 1968

L.C. McIntyre and W. Haeberli, Nucl. Phys. **A91** (1967) 382

G.L. Morgan, P.W. Lisowski, S.A. Wender, R.E. Brown, N. Jarmie, J.F. Wilkerson, and D.M. Drake Phys. Rev. C 33 , 1224 (1986)

H.W. Newson, E.G. Bilpuch, F.O. Purser, J.R. Boyce and T.B. Clegg, Nucl. Instr. Meth. 122 (1974) 99

G.G. Ohlsen, J.L. McKibben and G.P Lawrence, *Proceedings of the Third International Symposium on Polarization Phenomena in Nuclear Reactions* , p.503 (1971) (The University of Wisconsin Press, Madison,Wisconsin)

C.M. Perey and F.G. Perey, Atomic Data and Nuclear Data Tables Vol. 17, No. 1, 1976

C. Rolfs, Nucl. Phys. A217 (1973) 29

H.J. Rose and D.M. Brink, Rev. Mod. Phys. 39, No. 2 (1967) 306

R.G. Seyler and H.R. Weller, Phys. Rev. C 20 1979 453

D.M. Skopik et al, Phys. Rev. C 19 1979 601

M. Suffert, W. Feldman, J. Mahieux, and S.S. Hanna, Nucl. Instr. Meth. 63 (1968) 1

J.D. Turner, unpublished Ph.D. Dissertation, Duke University, 1978

H.R. Weller and N.R.Roberson, Rev. Mod. Phys. 52 4 (1980) 699

S.A. Wender, C.E. Floyd, T.B. Clegg, and W.R. Wylie, Nucl. Inst.Meth. 174 (1980) 341.

Biography

John Charles Riley

Born January 25, 1960 in Union, S.C.

Graduated from Union High School in Union, S.C. May,1978

Graduated Cum Laude from Furman University in May, 1982

Entered Duke University in September, 1982, in pursuit of a Ph.D.

Recieved A.M. degree from Duke in 1985

Married Grace Elena Mendez on September 12, 1987

Member American Physical Society

Publications:

Radiative capture of tensor and vector polarized deuterons by ^{3}H at 400 keV, J.C. Riley, H.R. Weller, Duke University and TUNL, D.R. Tilley, N.C. State University and TUNL, Physical Review C 40 (1989) 1517

Radiative capture of tensor and vector polarized deuterons by ^{3}H at 8.6 MeV and 400 keV, J.C. Riley, H.R. Weller, Duke University and TUNL, and D.R. Tilley, N.C. State University and TUNL, Proceedings of the Sixth Conference on Gamma-Ray Spectroscopy, Leuven, Belgium, 31 August - 4 September, 1987

Radiative capture of polarized deuterons by ^{3}H J.C. Riley, H.R. Weller, Duke University and TUNL, D.R. Tilley, N.C. State University and TUNL, Bulletin of the American Physical Society 32 (1987) 1547

Radiative capture of tensor polarized deuterons by ^{3}He and ^{3}H J.C. Riley, R.M. Whitton, H.R. Weller, Duke University and TUNL, and D.R. Tilley, N.C. State University and TUNL, Bulletin of the American Physical Society 30 (1985) 700